medRxiv preprint doi: https://doi.org/10.1101/2022.08.05.22278366; this version posted November 8, 2022. The copyright holder for this preprint (which was not certified by peer review) is the author/funder, who has granted medRxiv a license to display the preprint in perpetuity. It is made available under a CC-BY 4.0 International license .

Super-resolution imaging pinpoints ultrastructural changes at the node of Ranvier in patients with polyneuropathy

Luise Appeltshauser[1 *], Janis Linke[1,2 *], Hannah S. Heil[2,3 *], Christine Karus[2], Joachim Schenk[2], Katherina Hemmen[2], Claudia Sommer[1], Kathrin Doppler[1] ✉, and Katrin G. Heinze[2] ✉

[1]Department of Neurology, University Hospital Würzburg, Würzburg, Germany
[2]Rudolf Virchow Center, Center for Integrative and Translational Bioimaging, University of Würzburg, Würzburg, Germany
[3]Current affiliation: Optical Cell Biology, Instituto Gulbenkian de Ciência, Oeiras, Portugal
[*]these authors are co-first authors

To shed light on nanoscale pathologies in patients with polyneuropathy, we assessed human nerve biopsies by super-resolution fluorescence microscopy. We focused on both physiological protein arrangement and pathological ultrastructural changes at the node of Ranvier, a crucial region of the peripheral myelinated axon. Direct stochastic optical reconstruction microscopy (*d*STORM) revealed a ∼190 nm periodic protein arrangement of cytoskeletal proteins and axoglial cell adhesion molecules. Periodic distances increased at the paranodal region of the node of Ranvier in patients with polyneuropathy, both at the axonal cytoskeleton and at the axoglial junction. In-depth image analysis of human nerve biopsies revealed a partial loss of proteins of the axoglial complex (Caspr-1, neurofascin-155) in combination with detachment from the cytoskeletal anchor protein ß2-spectrin. Super-resolution dual-color colocalization data was supported by high-content confocal imaging combined with deep learning-based analysis, indicating that paranodal elongation occurs especially in acute and severe axonal neuropathy, as a possible correlate of Wallerian degeneration and related cytoskeletal damage. Our findings show that super-resolution imaging can identify, quantify and map elongated periodic protein distances in peripheral nerve biopsies for pathophysiological studies and direct implications for diagnostic assessment.

Super-resolution Microscopy | Polyneuropathy | Node of Ranvier

Correspondence:
Doppler_K@ukw.de & katrin.heinze@virchow.uni-wuerzburg.de

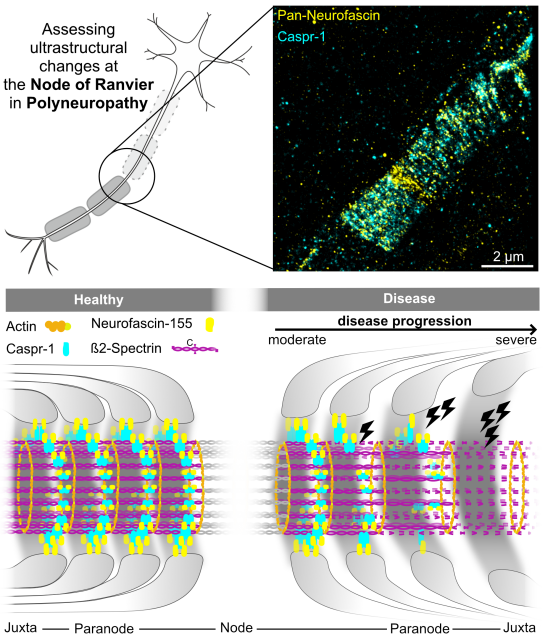

Graphical abstract: Pathological alterations of ultrastructural protein arrangement at the paranodal region of the node of Ranvier in polyneuropathy. Super-resolution microscopy allows for assessing ultrastructural protein arrangement and pathological alterations in patients with polyneuropathy. In human healthy nodes, axoglial and axoskeletal proteins follow a 190 nm periodic arrangement (left). In pathologically altered nodes (right), periodic protein distances of axonal ß2-spectrin elongate, in combination with elongation and partial loss of the axoglial complex of Caspr-1 and neurofascin-155. The axoglial complex itself colocalizes closely even in pathologically altered nodes. A complete loss of the axoglial complex could be the ultrastructural correlate of the detachment of paranodal myelin loops. Scale bar 2 µm.

Introduction

Polyneuropathies are the most common disorder of the peripheral nervous system (1). They are characterized by impaired signal transduction of peripheral nerves, resulting in severe sensorimotor deficits with high disability in affected patients (2). Different pathomechanisms involve axonal, myelin and Schwann cell damage. In recent years, the essential role of the node of Ranvier and the severe consequences of its alterations have come to focus (3, 4).

The node of Ranvier of myelinated axons is the key element for rapid long-distance neuronal signal transduction via saltatory conduction (5–7). Its highly organized nanostructure allows for clustering ion channels at the nodal region and securing cell adhesion at the paranodal and juxtaparanodal region (8–11). The complex Schwann cell - axon interplay is mediated by selected cell adhesion proteins at the paranode, like glial neurofascin-155 and axonal contactin-1 associated protein 1 (Caspr-1). They form part of the axoglial complex and attach the terminal myelin loops to the axon (6, 12, 13). In rodents, new super-resolution imaging techniques have shown that these cell adhesion molecules, and also ion channels and axonal scaffold proteins, are arranged following a ∼190 nm periodicity (14). Yet, little is known about the nanostructural protein arrangement of the node of Ranvier in humans, and especially in pathologically altered nerves.

Resolving such small protein periodicities would not be possible without the application of super-resolution microscopy, which provides an unpreceded insight into the molecular

NOTE: This preprint reports new research that has not been certified by peer review and should not be used to guide clinical practice.

medRxiv preprint doi: https://doi.org/10.1101/2022.08.05.22278366; this version posted November 8, 2022. The copyright holder for this preprint (which was not certified by peer review) is the author/funder, who has granted medRxiv a license to display the preprint in perpetuity. It is made available under a CC-BY 4.0 International license .

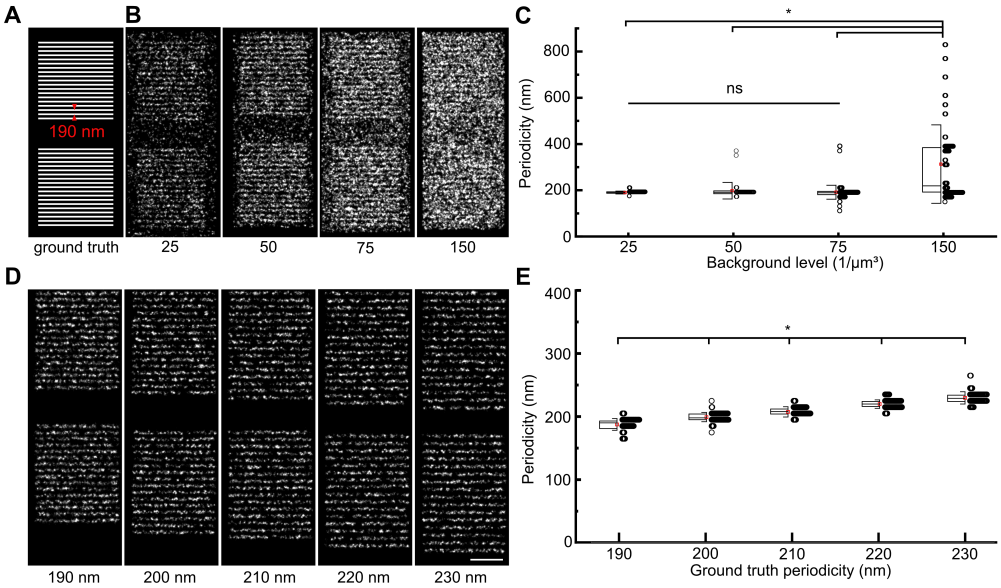

Fig. 1. Super-resolution image autocorrelation analysis reliably identifies structural periodicity. (A) The robustness of image autocorrelation analysis is tested on simulated Single Molecule Localisation Microscopy (SMLM) data based on a line structure with 190 nm periodicity as a ground truth. (B) For background levels ranging from 25 - 150 events/µm^3, autocorrelation recovers the underlying periodicity spacing as visualized in (C) boxplots, only failing at the highest background level (median ± standard deviation; 25: 190 ± 6 nm, n = 99; 50: 190 ± 36, n = 90; 75: 188 ± 30 nm, n = 143; 150: 218 ± 170 nm, n = 88; Kruskal-Wallis test with Dunn's correction for multiple testing). (D) For ground truth structures with periodicities varying from 190-230 nm, autocorrelation (E) successfully retrieves and clearly distinguishes the different periodicity spacings (median ± standard deviation; 190: 187.6 ± 9.3 nm; 200: 199.1 ± 7.4 nm; 210: 207.5 ± 8.1 nm; 220: 219.9 ± 6.6 nm; 230: 229.6 ± 9.9 nm; n=60 in all cases, Kruskal-Wallis test with Dunn's correction for multiple testing). Scale bar 1 µm.

organization and protein interaction in health and disease (15). Both Stimulated Emission Depletion (STED) and direct Stochastic Optical Reconstruction Microscopy (*d*STORM) (16, 17) combine target specificity with a very high spatial resolution and allow analysis of periodic ultrastructures by computational autocorrelation analysis (18, 19). In contrast to STED, *d*STORM in particular pinpoints molecular positions in cells and tissue with nanometer precision. With thousands of hits per image, *d*STORM provides maps of the subcellular architecture as a prerequisite for further analysis of molecular clusters, colocalization and relative positions (20–22). So far, super-resolution microscopy has mainly been applied to map the neuronal nanoscale anatomy under physiological (14, 23–26), but rarely under pathological conditions (27–29). Despite its potential for pathophysiological understanding and diagnostic assessment, *d*STORM has not been applied on human nerves.

Here, we apply *d*STORM to ex vivo human sensory nerve teased fiber preparations of patients with polyneuropathy, and analyze the nanoscale periodicity of selected adhesion and scaffold proteins at the node of Ranvier. To reveal underlying mechanisms of pathological alterations, we also assessed the interaction of the axoglial adhesion molecules neurofascin-155 and Caspr-1 and the axonal scaffold protein ß2-spectrin by dual-color colocalization analysis. To assess node of Ranvier morphometrics in parallel, a tailored high-content confocal imaging pipeline as a complementary modality was implemented. Considering histopathological acuteness, type and severity of the disease as well as clinical features in the analysis, we could relate our nanoscale findings to histopathological and clinical data, thereby exploring both pathomechanistic implications and the diagnostic potential of our methods.

Results

Definition and validation of histopathological categories of polyneuropathy. In order to assess the nodo-paranodal nanoscale organization in the human species and to identify possible pathological changes, we included n = 17 patients with polyneuropathy into our study. These had undergone sensory nerve biopsy (n = 16 sural nerve, n = 1 radial superficial nerve) during the routine diagnostic workup process. Demographic data and electrophysiological and clinical diagnosis including diagnostic criteria are listed in Supporting Table S1. An experienced examiner made the histopathological diagnosis from standard histological stains, and classified according to the primarily affected structure (axonal / demyelinating), the acuteness (acute / chronic) and the severity of axonal loss (mild / moderate / severe; see Supporting Table S2). Histopathological and clinical parameters differed significantly in acute vs. chronic and axonal vs. demyelinating neuropathy. Furthermore, electroneurographic features of the respective sensory nerve correlated to the histopathological severity of axonal loss. The nerve fiber density was significantly reduced in acute vs. chronic neuropathy (see Supporting Table S3 and Supporting Fig. S1). Accordingly, we separated our patients into three histopathological subcohorts: acute axonal neuropathy (n = 6 patients), chronic axonal neuropathy (n = 6 patients) and chronic demyelinating neuropathy (n = 5 patients). This allowed for a direct comparison of ultrastructural changes in nodo-paranodal nanoscale organization in relation to type, acuteness and severity of neuropathy.

Development and validation of a *d*STORM autocorrelation analysis tool. Patient derived tissue preparations pose a whole set of challenges for super-resolution imaging. Es-

medRxiv preprint doi: https://doi.org/10.1101/2022.08.05.22278366; this version posted November 8, 2022. The copyright holder for this preprint (which was not certified by peer review) is the author/funder, who has granted medRxiv a license to display the preprint in perpetuity. It is made available under a CC-BY 4.0 International license .

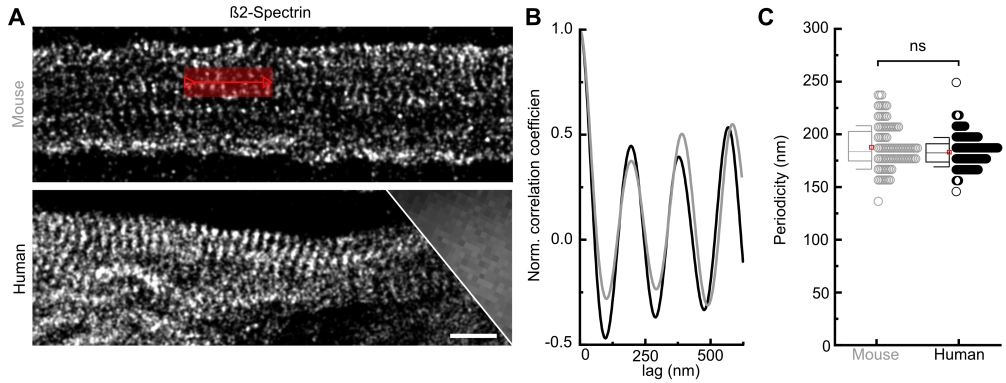

Fig. 2. Super-resolution image autocorrelation analysis resolves the periodic cytoskeletal ultrastructure at the internode in rodents and humans. (A) *d*STORM resolves the longitudinal periodic arrangement (red arrow) of internodal ß2-spectrin in teased fiber preparations of murine (top) and human (bottom) axons, in contrast to conventional diffraction-limited widefield microscopy (inset, right). (B) Oscillating normalized correlation coefficient curves show equal ∼190 nm peak-to peak distances and thus an equal periodic arrangement of murine (gray) and human (black) axonal ß2-spectrin. (C) Boxplots of the distribution of periodic spacings measured by the autocorrelation analysis in murine (n = 99) and human teased fiber preparations (n = 192) show no significant differences in median periodic arrangement between the two species, tested by Mann-Whitney test. Boxplots display mean (red square), median (line), standard deviation (whiskers) and 25-75% (box). Scale bar 1 µm.

pecially a limited immunolabeling efficiency and nonspecific binding can compromise the image reconstruction quality and resolution. To retrieve the periodic arrangement of structural proteins in the internodal and paranodal region in patient derived tissue samples with *d*STORM microscopy, we developed a custom and easy-to-use image analysis tool implemented in MatLab (Mathworks Inc.). This tool is based on image autocorrelation of selected regions of interest within the super-resolved reconstructions, and allows for directly retrieving the periodicity of a certain protein ring structure from peak-to-peak distances in its respective autocorrelation profile. The general image processing workflow is illustrated in Supporting Fig. S2. We validated the performance and robustness of our approach using simulated datasets. To define a ground truth model for our simulations, we assumed a previously described 190 nm periodic arrangement of paranodal proteins (14) (Figure 1 A) and tested whether the image autocorrelation approach can achieve high levels of accuracy and robustness even in the challenging conditions presented in this study. As a result, we could reliably detect the ground truth of a 190 nm periodic arrangement in a simulated datasets despite high background levels and strongly reduced marker densities (Figure 1 B,C, and Supporting Fig. S3). Changes in the periodicity could be distinguished clearly, respectively (Figure 1 D,E).

The adult human axonal internodal scaffold follows a ∼190 nm periodic arrangement. Next, we implemented the autocorrelation analysis on super-resolved *d*STORM image reconstructions of murine and human teased fiber preparations, significantly increasing the resolution in comparison to diffraction-limited microscopy (Figure 2A, inlet). First, we studied the periodicity of the internodal axoskeleton. In mice, we were able to display a periodic arrangement of ß2-spectrin, with a mean periodic distance of 188 nm, thus corresponding to previously described data (30). In human sural nerves, we found a mean periodicity of 184 nm, without significant difference to periodic distances in rodents (Figure 2 B and C, detailed values are shown in Supporting Table S4). Thus, the ∼190 nm structural protein periodicity is conserved in human adults.

Disruption of the ultrastructural periodic arrangements of paranodal proteins in patients with polyneuropathies. We then addressed the ultrastructural protein arrangement in the paranodal region of the node of Ranvier in rodents and humans. First, we analyzed the periodicity of axonal cytoskeletal ß2-spectrin in the paranodal compartment. In contrast to the internodal segment, the ultrastructural arrangement of ß2-spectrin was altered at the paranodal axon in patients with axonal neuropathies (see Figure 3 A, C, E). We could detect a significant increase of the periodicity of ß2-spectrin at the paranode in patients with axonal neuropathies compared to rodents (202 vs. 184 nm, $p = 0.002$). In patients with demyelinating neuropathies, however, the paranodal ß2-spectrin periodicity did not differ significantly from rodents (191 vs. 184 nm, $p = 0.78$). Differences in the periodicity between patients with axonal and demyelinating disease were not significant (see Supporting Table S4). Next, we assessed the paranodal axoglial junctional protein Caspr-1, located at the axon together with contactin-1 and tethered to axonal ß2-spectrin through protein 4.1B, and the glial binding partner of contactin-1, neurofascin-155 (9, 13, 31–33). The mean periodic distance of the axonal cell adhesion molecule Caspr-1 was severely elongated in patients with axonal and demyelinating neuropathy compared to rodents (247 ± 99 nm vs 187 ± 25 nm, $p < 0.0001$, see Figure 3 B,D,F and Supporting Table S4). The same applied for its glial counterpart neurofascin-155 (284 ± 125 nm vs. 173 ± 24 nm, $p < 0.0001$, see Figure 3 F and Supporting Table S4). In our patient samples, we observed a broad distribution of spacings that ranged from "healthy" nodes (with physiological periodic arrangement) to highly pathological nodes or heminodes (with disturbed periodicity). Figure 3 D illustrates that pathological alterations of the paranodal nanostructure follow a longitudinal direction, from the node to the internodal axon. This mid-to-lateral increase in periodic protein distance could be the correlate of a loosening of the helical Caspr-1 coils in pathologically altered nodes of Ranvier. In summary, *d*STORM was able to detect pathological alterations of the paranodal periodic protein arrangement in polyneuropathy in general, but especially on the level of individual nodes and patients,

medRxiv preprint doi: https://doi.org/10.1101/2022.08.05.22278366; this version posted November 8, 2022. The copyright holder for this preprint (which was not certified by peer review) is the author/funder, who has granted medRxiv a license to display the preprint in perpetuity. It is made available under a CC-BY 4.0 International license .

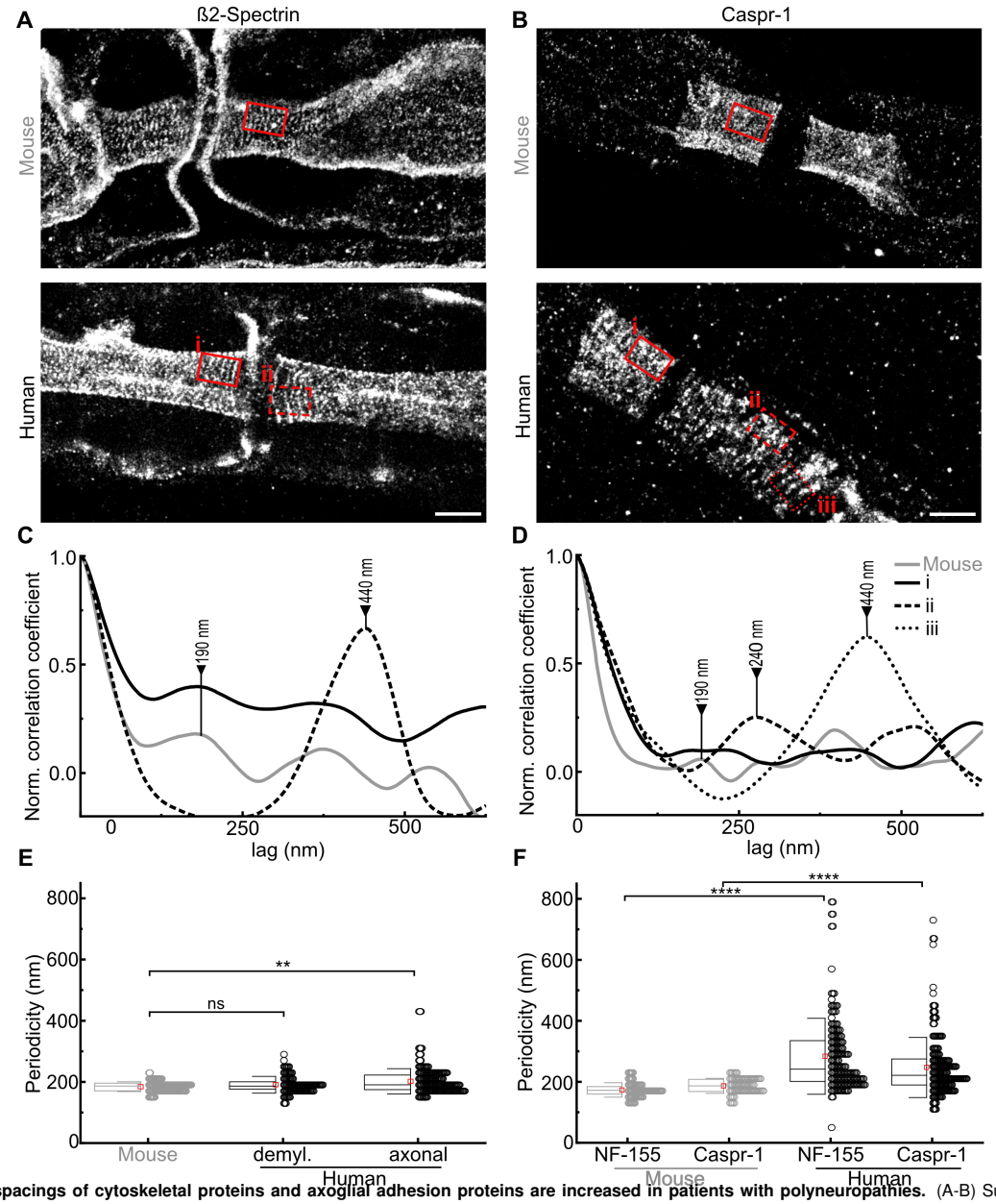

Fig. 3. Periodic spacings of cytoskeletal proteins and axoglial adhesion proteins are increased in patients with polyneuropathies. (A-B) Super-resolved image reconstruction of (A) cytoskeletal ß2-spectrin and (B) axonal adhesional Caspr-1 organization at the node of Ranvier in teased fiber preparations of murine (top) and human (bottom) ex vivo axons. (C-D) Autocorrelation coefficient curves of the image regions marked in red in (A-B) of the distribution of ß2-spectrin (C) and Caspr-1 (D) in murine (gray lines) and human (black lines) teased fiber preparations indicating a local extension of the observed periodicity in pathological affected paranodes (dashed and dotted lines). (E) Boxplots of the distribution of periodic spacings of paranodal ß2-spectrin measured by autocorrelation analysis in mice (n = 130) and patients with histopathologically demyelinating (demyl., n = 106) and axonal (n = 159) neuropathy show a significant increase in cytoskeletal ß2-spectrin periodic arrangement in patients with axonal neuropathy, but not with demyelinating neuropathy. (F) Boxplots of the distribution of periodic spacings of Caspr-1 and neurofascin-155 (NF-155) in mice (n = 80 & 92) and in patients (n=194 & 173) show a highly significant increase in periodic spacings of axoglial proteins in patients with all types of polyneuropathies, with high variance between single regions of interest. Kruskal-Wallis test with Dunn's correction for multiple testing was used for comparison. Significance level: * $p < 0.05$, ** $p < 0.01$, *** $p < 0.001$, **** $p < 0.0001$. Boxplots display mean (red square), median (line), standard deviation (whiskers) and 25-75% (box). Scale bars 2 µm.

thus demonstrating its potential diagnostic aptitude to assess nanoscale pathology in selected patients.

The axoglial complex remains attached even in pathologically altered nerves . We performed a colocalization analysis of Caspr-1, neurofascin-155 and ß2-spectrin on drift-corrected dual-color *d*STORM datasets of murine and human teased nerve fibers and quantitatively assessed colocalization with Manders' A and B coefficients (34, 35). In mice, axonal Caspr-1 colocalized perfectly both with its glial counterpart neurofascin-155, as well as with its cytoskeletal anchor ß2-spectrin, represented by high Manders' coefficients (Figure 4 A, B, E, F and Supporting Table S4). In human samples, on the other hand, colocalization of axonal Caspr-1 with the paranodal fraction of cytoskeletal ß2-spectrin was disrupted in patients with axonal and demyelinating polyneuropathies, represented by significantly reduced Manders' A and B coefficients, with partial loss of Caspr-1 alongside alterations of the cytoskeletal periodic arrangement (Figure 4 D, F). Still, our data indicated an integrity of the paranodal axoglial complex of Caspr-1 and neurofascin-155, even if nodo-paranodal architecture was severely disrupted: Despite a partial loss of

medRxiv preprint doi: https://doi.org/10.1101/2022.08.05.22278366; this version posted November 8, 2022. The copyright holder for this preprint (which was not certified by peer review) is the author/funder, who has granted medRxiv a license to display the preprint in perpetuity. It is made available under a CC-BY 4.0 International license .

Category	node/tissue volume (1/mm^3)	paranodal axonal diameter (µm)	nodo-paranodal length (µm)	nodal length (µm)
intact human nodes	n.a.	2.3 ± 0.9.	10.0 ± 4.9.	0.9 ± 0.3.
acute axonal neuropathy	16.1 ± 3.5	2.3 ± 0.9 n.s.	15.4 ± 10.1 ***	1.3 ± 1.4 n.s.
chronic axonal neuropathy	33.3 ± 10.0	2.2 ± 0.9 n.s.	12.6 ± 7.1 ****	1.2 ± 2.0 n.s.
chronic demylenating neuropathy	35.9 ± 26.6	2.7 ± 1.0 **	12.9 ± 7.1 ****	1.1 ± 0.9 n.s.
murine sural nerve	77.2	1.9 ± 0.44 n.s.	8.8 ± 1.5 n.s.	1.1 ± 0.44 n.s.

Table 1. Nodo-paranodal morphometrics in murine and human sensory nerves - physiological and pathological conditions. The table displays means ± standard deviations (SD) of nodo-paranodal parameters (nodo-paranodal length, nodal length and paranodal axonal diameter) measured on Caspr-1 staining in human sural nerve intact nodes of Ranvier, and nodes of Ranvier of patients classified as acute axonal, chronic axonal and chronic demyelinating neuropathy (>180 nodes per cohort). Adjusted p-values are displayed compared to intact human nodes using Kruskal-Wallis test with Dunn's correction for multiple testing. Individual patient values and n numbers are displayed in Supplemental Table S5. Significance levels: * $p < 0.05$, ** $p < 0.01$, *** $p < 0.001$, **** $p < 0.0001$. Abbreviations: n.a = not applicable, n.s. = not significant, SD = standard deviation.

Caspr-1/ neurofascin-155 staining at the paranode, Manders' A and B correlation coefficients did not decrease compared to murine samples in patients with demyelinating, chronic axonal and acute axonal neuropathies (see Figure 4 C, E and Supporting Table S4). In conclusion, our data indicate that axoskeletal alterations could contribute to lateral diffusion and loss of the axoglial complex at the paranodes, as the junctional complex itself remains closely attached even in pathologically altered nodes.

High content confocal imaging reveals physiological nodo-paranodal parameters and identifies the node of Ranvier density as surrogate parameter for axonal loss. To relate our findings on a nanoscale level to the analysis of a higher number of nodes per patient, to "capture the bigger picture" of node of Ranvier pathology in patients with polyneuropathies of different etiologies and to evaluate the diagnostic potential of teased fiber immunofluorescence imaging, we performed high-content confocal imaging including large field of view photomicrographs on triple-stained teased fiber preparations and assessed the number of nodes of Ranvier and morphometrics in relation to type and stage of neuropathy. As data are scarce, we firstly defined normal values of nodo-paranodal parameters measured on sural nerves of human adults, as shown in Figure 5 A-B and the Supporting Movie M1. The mean nodo-paranodal length was 10.0 ± 4.9 µm, the mean nodal length in humans was 0.9 ± 0.3 µm and the axonal paranodal diameter was 2.3 ± 0.9 µm, without any significant differences to murine sural nerve parameters (see Table 1). These values can be considered as normal values of unaltered nodes of Ranvier in adult humans. Next, to check whether the teased fiber samples represented type and severity of neuropathy as assessed by cross-sectional gold standard analysis, we measured the node of Ranvier density per tissue volume on each sample by manual counting and by the application of deep learning strategies (see Supporting Notes 2 and 3). Counting accuracy using a fully automated deep learning approach was 1.21 ± 0.77 in human samples, with a highly significant correlation to manual assessment (see Supporting Note 3 and Figure S4). Patients with acute axonal neuropathy showed a significantly reduced nodal count compared to patients with chronic axonal neuropathy and chronic demyelinating neuropathy (16.1 vs. 33.3 vs. 35.9, p = 0.010 and p = 0.037, see Figure 5 C). We found a strong correlation of the total count of nodes of Ranvier in our teased fiber samples with parameters assessed by gold standard cross-sectional analysis: Teased fiber node density correlated with the semi-quantitative rating of histopathological severity of axonal loss (Spearman r = -0.75, $p < 0.0001$), the mean fiber density as an exact quantification of histopathological severity of axonal loss (Spearman r = 0.68, p = 0.002, see Figure 5 D) and with the mean count of Wallerian degeneration figures (Spearman r = -0.54, p = 0.026). Thus, we confirmed that our teased fiber preparations were representative of the histopathological diagnoses. Furthermore, we showed that the node of Ranvier density in teased fiber preparation is a possible surrogate marker for the severity of axonal loss that can be assessed accurately in human samples for diagnostic purposes by the application of deep learning strategies.

Dispersion of the paranodal junctional complex in patients with acute and severe axonal neuropathy. Next, we assessed nodo-paranodal parameters of > 180 nodes per cohort in patients classified as acute axonal, chronic axonal and chronic demyelinating neuropathy. We found a significant increase in nodo-paranodal length in all three groups compared to intact human nodes (see Figure 6 A-B). Particularly notable is that we detected apparent differences within single patients and histopathological categories: Patients with acute axonal damage showed significantly increased nodo-paranodal length compared to patients with chronic axonal polyneuropathy (15.6 vs. 12.4 µm, p = 0.002). Results closely missed significance compared to patients with demyelinating polyneuropathy (15.6 vs. 12.9 µm, p = 0.06, see Figure 6 B). Additionally, nodo-paranodal length was significantly increased in patient samples with histopathologically severe axonal loss compared to moderate (16.8 vs. 12.8, p = 0.0018) and mild axonal loss (16.8 vs. 12.9, p = 0.0022, see Figure 6 C). Interestingly, single patients showed severe and highly significant nodo-paranodal alterations, especially in the cohort of acute axonal neuropathy, whereas other patients showed nodo-paranodal lengths without significant differences to normal values (individual data are shown in Supporting Table S5). Furthermore, we compared nodo-paranodal lengths between patients fulfilling diagnostic criteria for diseases with different underlying pathophysiology: 1) Vasculitic neuropathy with primarily axonal damage and

medRxiv preprint doi: https://doi.org/10.1101/2022.08.05.22278366; this version posted November 8, 2022. The copyright holder for this preprint (which was not certified by peer review) is the author/funder, who has granted medRxiv a license to display the preprint in perpetuity. It is made available under a CC-BY 4.0 International license .

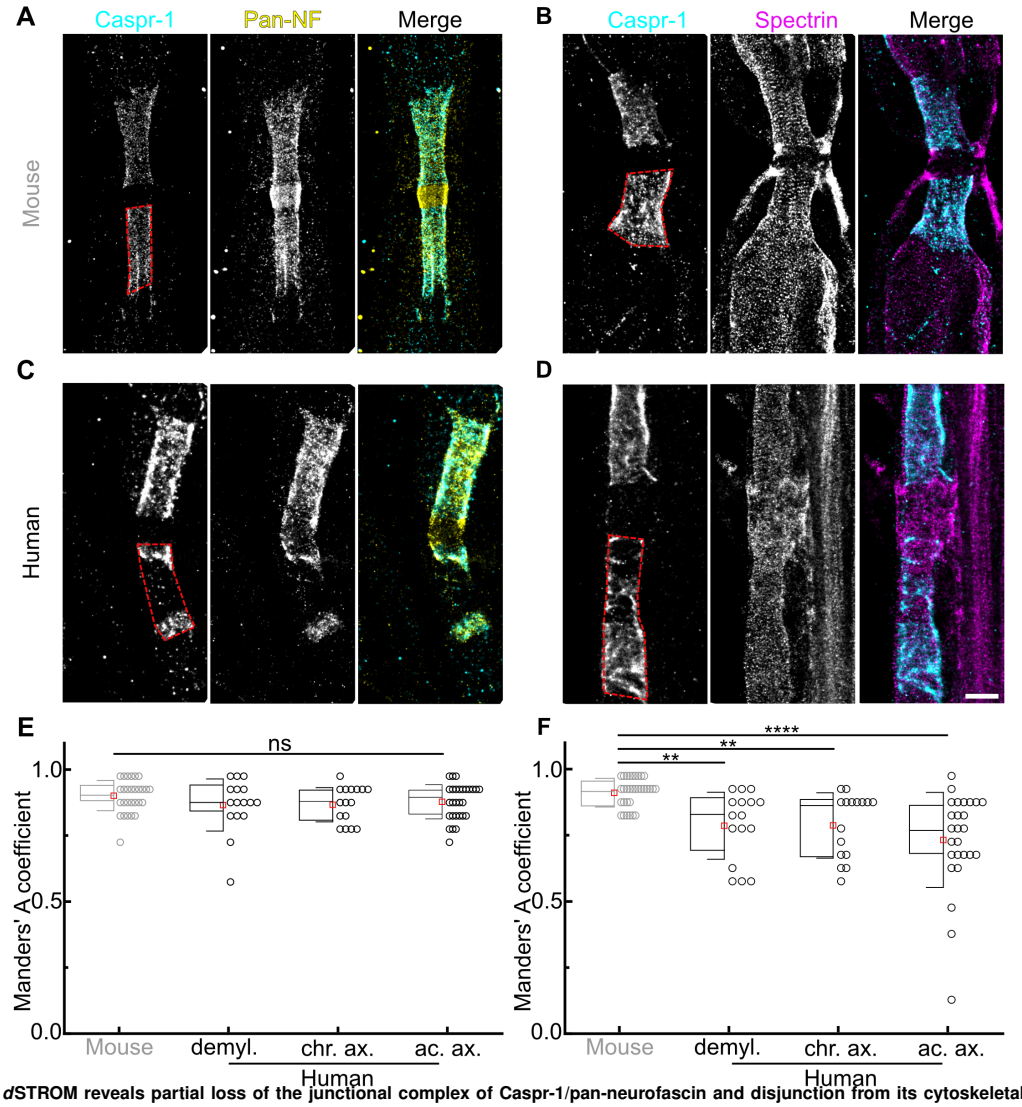

Fig. 4. Dual-color *d*STROM reveals partial loss of the junctional complex of Caspr-1/pan-neurofascin and disjunction from its cytoskeletal anchor protein ß2-spectrin in polyneuropathy. (A-D) Super-resolved image reconstruction show colocalization of Caspr-1 (cyan) and pan-neurofascin (Pan-NF, yellow; A, C) and Caspr-1 and ß2-spectrin (magenta; B, D) in murine (A-B) and human (C-D) teased fiber preparations. Exact colocalization appears white. Gaps within the paranodal Caspr-1/pan-neurofascin staining illustrate partial loss of the axoglial complex at the paranode in a patient with acute and severe axonal neuropathy (C). Note: neurofascin-staining in the nodal region was not considered in the analysis, as the pan-neurofascin antibody stains both paranodal neurofascin-155 and nodal neurofascin-186 isoform. Analysis was performed within the paranodal region only (red dashed line). (D) In areas of loss of axonal Caspr-1, ß2-spectrin staining is still present, but pathologically altered without clearly visible periodic arrangement. (E) Boxplots show the distribution of Manders' correlation coefficients between the axoglial complex Caspr-1 and neurofascin-155 in murine paranodes (n = 28) and paranodes of patients with demyelinating (demyl. n = 16), chronic axonal (chr.ax., n = 16) and acute axonal (ac.ax., n=28) neuropathy, without significant differences between the groups. (F) The distribution of Manders' correlation coefficients between axonal junctional Caspr-1 and cytoskeletal anchor protein ß2-spectrin in the same groups (n = 32 / 16 / 16 / 26 paranodes) show significantly decreased colocalization and thus a detachment of Caspr-1 from its anchor molecule, especially in the group of acute axonal neuropathies. Testing was performed using Kruskal-Wallis with Dunn's correction for multiple testing. Significance level: * $p < 0.05$, ** $p < 0.01$, *** $p < 0.001$, **** $p < 0.0001$. Boxplots display mean (red square), median (line), standard deviation (whiskers) and 25-75% (box). Scale bars 2 µm.

distal Wallerian degeneration due to ischemia and 2) chronic inflammatory demyelinating polyradiculoneuropathy (CIDP) affecting the internodal myelin. Nodo-paranodal length was significantly longer in patients with vasculitic neuropathy compared to CIDP (13.2 ± 6.8 vs. 12.3 ± 6.4 µm, $p = 0.036$). Thus, an increase in nodo-paranodal length was identified as an indicator for acute and severe axonal damage during Wallerian degeneration, and high inter-individual differences highlight possible distinct underlying pathologies and the diagnostic potential of the method. Results on further morphometric parameters and their relation to clinical information are described in the Supporting Note 4. In conclusion, the results from the high-content analysis of teased fiber samples labeled with standard immunofluorescence add to and support our findings on an ultrastructural level assessed by super resolution *d*STORM: The nodes assessed by *d*STORM were representative within the samples and diagnostic categories, and we showed that nodo-paranodal alterations occur at a severe level especially in acute and severe axonal neuropathy. By *d*STORM, we could identified the alteration of the axonal cytoskeletal ultrastructure as a possible pathogenic link to dispersion and loss of the paranodal axoglial complex in acute axonal neuropathies. A summarizing schematic display is presented in the graphical abstract (p.1).

Discussion

Here, we implement *d*STORM imaging on human tissue, map physiological axonal ultrastructure in humans and iden-

medRxiv preprint doi: https://doi.org/10.1101/2022.08.05.22278366; this version posted November 8, 2022. The copyright holder for this preprint (which was not certified by peer review) is the author/funder, who has granted medRxiv a license to display the preprint in perpetuity. It is made available under a CC-BY 4.0 International license .

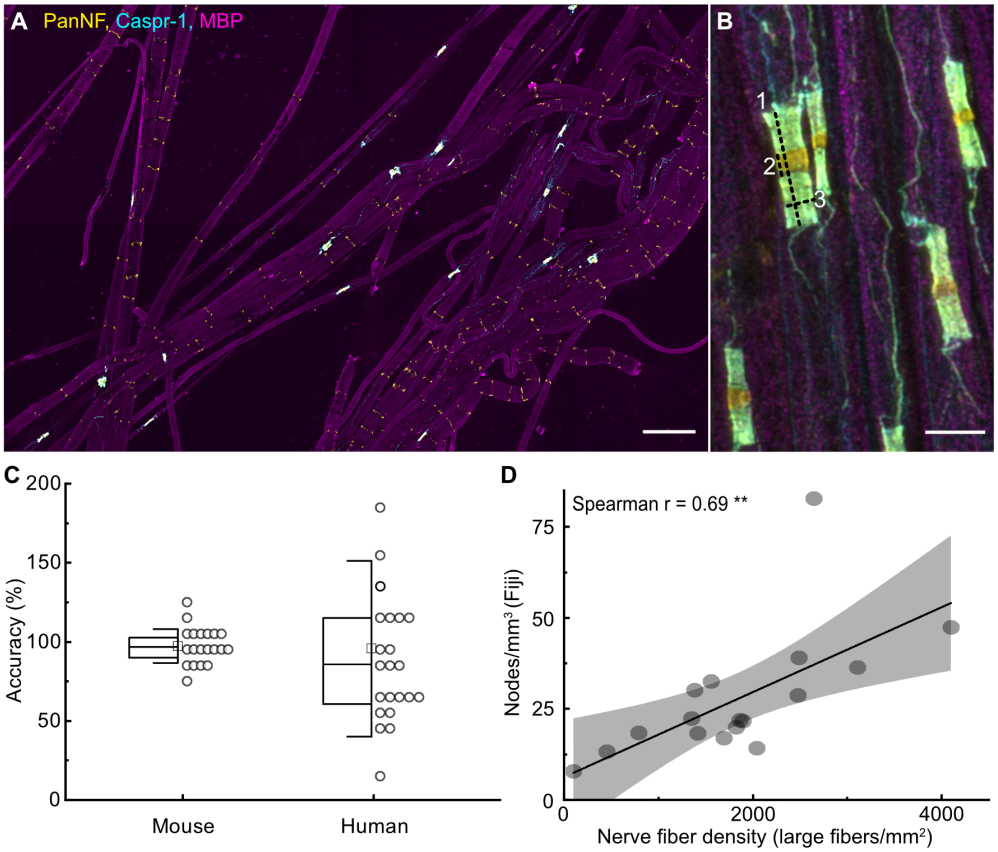

Fig. 5. Assessing nodo-paranodal morphometrics and nodal count in large field of view photomicrographs. (A) large field of view photomicrographs of bundle teased fiber preparations of murine sural nerves show healthy myelinated fibers (MBP staining, magenta) with nodes of Ranvier expressing neurofascin-155 and neurofascin-186 (pan-neurofascin, yellow) and Caspr-1 (cyan), with colocalization at the paranode (white). Scale bar = 50 µm. (B) Nodo-paranodal morphometrics including nodo-paranodal length (1), nodal length (2) and axonal diameter (3) were assessed as indicated. Scale bar = 5 µm. (C) Accuracy of automated vs. manual node of Ranvier counting are shown for murine samples and human samples. In murine samples, automated analysis resulted in highly accurate results, whereas accuracy in human samples was reduced due to pathological node of Ranvier alterations. (D) The scatter plot shows a positive correlation of the teased fiber node of Ranvier density assessed manually with FIJI and the nerve fiber density assessed by gold-standard cross-sectional analysis in the whole cohort (Pearson r = 0.69, p = 0.002). Significance level: * p < 0.05. ** p < 0.01, *** p < 0.001, **** p < 0.0001.

tify distinct pathologies at the node of Ranvier on a nanoscale level in polyneuropathy. We demonstrate a physiological ∼190 nm periodic arrangement of the membrane-associated cytoskeleton that was disrupted in patients with polyneuropathy, exclusively at the paranodal region. Our data indicate that cytoskeletal alterations during Wallerian degeneration might facilitate nodo-paranodal detachment. We identify nanoscale pathologies in individual patients and thereby introduce single molecule localization microscopy as a potential method to enhance diagnostics of neurological diseases.

The ultrastructural paranodal protein arrangement is impaired in polyneuropathy. We report an increase in periodic distance of the axoglial cell adhesion molecules Caspr-1 and neurofascin-155 in patients with polyneuropathies. These proteins are components of the septate-like junctions at the paranodal region and are crucial for the integrity of the node of Ranvier and saltatory conduction (6, 9, 13). Previous studies have proposed a helical arrangement of Caspr-1 along the axon (36, 37). Here, we show a lateral increase in the periodic distance of Caspr-1 as a correlate of a lateral de-coiling of the axonal Caspr-1 helices in polyneuropathy.

Dual-color super-resolution imaging reveals distinct pathomechanisms of paranodal disjunction. To address the origin of the decoiling of the axoglial complex, we performed dual-color colocalization studies on *d*STORM image reconstructions. Our data show that the axoglial complex of Caspr-1 and neurofascin-155 itself is robust against disjunction, even in pathologically altered paranodes. We observed either physiological paranodal axoglial arrangement, equally increased periodicity or a partial loss of both proteins in parallel. Correspondingly, previous studies using rodent models have shown a close attachment of Caspr-1 to neurofascin-155 during myelination and in demyelinating conditions (37, 38). Thus, the disruption of the nodo-paranodal architecture in classical demyelinating and axonal polyneuropathy does not occur due to a primary disjunction of the axoglial contact, which is in contrast to antibody-mediated nodo-paranodopathies (see Supporting Note 5). Importantly, our data indicate that the paranodal region constitutes an Achilles' heel for cytoskeletal damage in axonal neuropathies. At the internode, we found no differences on internodal ß2-spectrin periodicity between humans and rodents. Our data thus are in line with previous studies that postulated that the axoskeletal ultrastructure follows a 190 nm periodicity and is conserved within species (25, 26, 30, 39).

medRxiv preprint doi: https://doi.org/10.1101/2022.08.05.22278366; this version posted November 8, 2022. The copyright holder for this preprint (which was not certified by peer review) is the author/funder, who has granted medRxiv a license to display the preprint in perpetuity. It is made available under a CC-BY 4.0 International license .

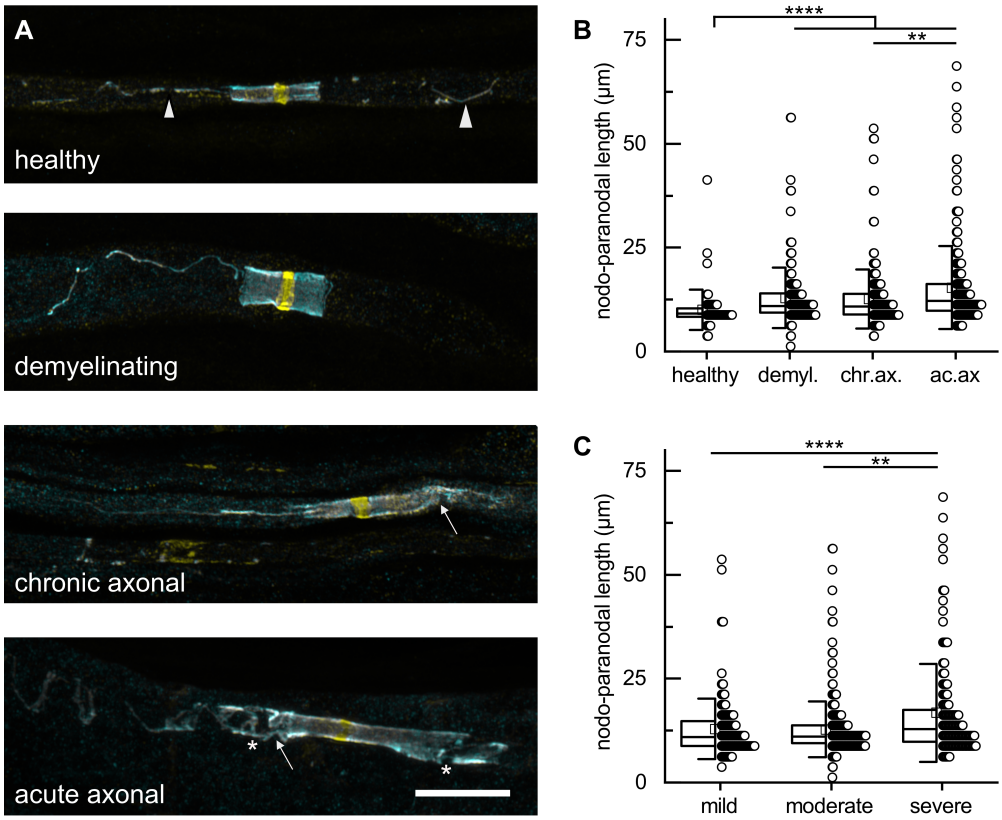

Fig. 6. Nodo-paranodal length is elongated with patients with acute and severe axonal neuropathy. (A) High magnification photomicrographs show node and paranode morphology in human nodes of Ranvier considered as unaltered and in patients classified as demyelinating, chronic axonal and acute axonal neuropathy. In physiological nodes, paranodal Caspr-1 (cyan) and neurofascin (yellow) are dense, and the mesaxon can be distinguished clearly (arrowheads). In patients with chronic and acute axonal neuropathy, paranodal elongation with decoiling of paranodal axoglial proteins (arrows) and partial loss of staining (asterisks) is visible. Correspondingly to results of *d*STORM analysis, Caspr-1 and neurofascin colocalize at the paranode (white), even in pathologically severely altered nodes of Ranvier. Scale bar = 10µm. (B) Nodo-paranodal length (µm, y-axis) is elongated in patients with all types of polyneuropathies compared to unaltered human nodes, especially in patients with acute axonal neuropathy. (C) Nodo-paranodal length (µm, y-axis) is elongated in patients with histopathologically severe axonal loss, compared to mild and moderate axonal loss. Testing was performed using Kruskal-Wallis with Dunn's correction for multiple testing. Significance level: * $p < 0.05$. ** $p < 0.01$, *** $p < 0.001$, **** $p < 0.0001$.

At the paranode, on the other hand, we observed an increase in periodic arrangement of ß2-spectrin in patients with polyneuropathy compared to rodents. We exclusively studied ß2-spectrin, as other cytoskeletal proteins like F-actin and ankyrin B are also present in the paranodal glial terminal loops, and their complex 3D structure impede the analysis of axonal periodicity (14). The paranodal region might be prone to cytoskeletal alterations for two main reasons: Firstly, the axon diameter is reduced, axoskeletal transport proteins are condensed and axonal transport rates are reduced at the paranode (40, 41). Endogenous metabolites could therefore accumulate, leading to axoskeletal damage. Secondly, the node of Ranvier is less protected by the myelin sheath and thus exposed to exogenous noxious and inflammatory agents, leading to cytoskeletal alterations (42). Rodent electron microscopy studies have shown that Wallerian degeneration begins at the nodal and paranodal axon, with accumulation of cell organelles and loosening of neurofilaments (43–45). Here, we show that the paranodal axon is the initial site of Wallerian degeneration in human disease, and provide evidence for specific cytoskeletal alterations at a nanoscale and protein level in patients with axonal neuropathy as a correlate of a beginning Wallerian degeneration.

Super-resolution imaging visualizes the link of paranodal detachment with cytoskeletal damage. Our findings imply that in axonal neuropathies, the paranodal cytoskeletal damage might be associated with the nodo-paranodal detachment. Previous studies including *d*STORM data suggest that a2/ß2-spectrin serves as an intra-axonal barrier, is crucial for the clustering of sodium channels at the node, for maintaining the periodicity of the membrane-associated cytoskeleton, and for axon survival (29, 46, 47). Here, we show that along with the alteration of the axonal cytoskeleton, the colocalization of Caspr-1 and its axonal anchor is severely disrupted. This finding implies that the alteration of cytoskeletal structure proteins might lead to a lateral decoiling of the Caspr-1 helices along the axon. This is in line with reports of a paranodal disorganization and decreased expression levels of Caspr-1 in protein 4.1B murine knockout models (32, 48, 49). As we can show that Caspr-1 and glial Neurofascin-155 attach strongly even if pathologically altered, we propose that Caspr-1 decoiling and loss might cause a broadening and detachment of the paranodal loops from the axon, with paranodal lengthening as a consequence. Correspondingly, we found a correlation of nodo-paranodal length to histopathological severity and acuteness of axonal loss. In line with these findings, early ultrastructural studies reported terminal loop alterations after cytoskeletal changes

medRxiv preprint doi: https://doi.org/10.1101/2022.08.05.22278366; this version posted November 8, 2022. The copyright holder for this preprint (which was not certified by peer review) is the author/funder, who has granted medRxiv a license to display the preprint in perpetuity. It is made available under a CC-BY 4.0 International license .

during Wallerian degeneration (43, 44). Paranodal detachment was previously reported in other neuropathies classified as axonal, such as diabetic neuropathy or chronic idiopathic axonal neuropathy (50, 51). Interestingly, patients of our cohort with primarily axonal pathology such as vasculitic neuropathy showed an increased nodo-paranodal length compared to CIDP, a disease characterized by internodal demyelination. Previously, Caspr-1 staining was proposed as a diagnostic marker to distinguish chronic idiopathic axonal neuropathy from CIDP, in line with our findings (51). Still, the conditional murine knockout of single axoskeletal molecules, even ß2-spectrin, does not lead to a complete detachment of Caspr-1, previously shown by using diffraction-limited microscopy (7, 46). Therefore, we suggest that a paranodal disjunction in axonal neuropathy occurs in case of a severe disruption of the axonal cytoskeleton involving several structure proteins at a time, and can better be observed using super-resolution imaging. Further studies are needed to address various cytoskeletal proteins, especially investigating the role of protein 4.1B (31, 48, 49), which was not included in the study due to a lack of a commercial antibody apt for super resolution microscopy. In summary, our data indicate that a paranodal elongation and disruption may rather be considered a secondary effect of axonal damage than a primarily demyelinating feature in axonal neuropathy. Via a combination of *d*STORM and high content confocal imaging, we could show that acute Wallerian degeneration with consecutive cytoskeletal damage could lead to dispersion of proteins of the axoglial complex and paranodal detachment.

Advanced high- and super-resolution microscopy pushes the boundaries of diagnostic assessment of nerve biopsies in polyneuropathies. Using a high-content confocal imaging approach, we were not only able to confirm our histopathological findings on an ultra-structural level in high sample sizes, but also provide a protocol of possible future use in the diagnostic work-up of polyneuropathies. Single teased fiber analysis, electron microscopy or longitudinal sections are well-established methods to examine the node of Ranvier, additionally to gold-standard cross-sectional analysis (52–55). Still, these methods can be time-consuming, require high expertise due to non-standardized assessment, depend on rater-dependent accuracy and partly do not allow to specifically study single proteins of interest (52–54, 56). Here, we introduce a different protocol including fiber bundle teasing that can be performed within 60 minutes, followed by triple immunofluorescence staining and automated confocal high-content image acquisition. This method yields the opportunity to study numerous nodes of Ranvier at high magnification, with easy navigation within the sample due to automated identification of regions of interest, and could reduce selection bias by the examiner. Furthermore, we applied basic deep learning algorithms on teased fiber preparations to assess nodal count and nodo-paranodal length, which was previously only reported in rodent samples and human cross-sectional tissue (see Supporting Note 3). Further development of these methods in future studies may set the basis for modern image analysis and quantification approaches to enhance histopathologic assessment of polyneuropathy. Furthermore, the imaging routine implemented in this study could in the future be transferred to less invasive diagnostic samples, such as skin punch biopsies, or to samples beyond neuropathies. We report standardized normal values of human adult sensory nerve nodo-paranodal length that had previously only been defined in children (57), and identify the node of Ranvier density as a surrogate marker for axonal loss in teased fiber preparations. Thus, we provide a method to assess both severity of axonal neuropathy and node of Ranvier pathology using one single application. Larger studies with homogenous cohorts need to confirm if nodo-paranodal morphometrics and ultrastructural assessment via *d*STORM can serve as diagnostic markers and assess their sensitivity, specificity and practicability in routine assessment.

In conclusion, our data contribute to the understanding of underlying node of Ranvier pathologies of peripheral neuropathies on a nanoscale level, and highlight the potential of advanced high and super-resolution microscopy for both diagnostics and pathophysiological studies. Our findings could pave the way for introducing new imaging techniques and super resolution microscopy into histopathologic diagnostic assessment of patients with neurologic conditions.

Data availability. Data as described above are available here: https://doi.org/10.5281/zenodo.6387771. Further raw data including original photomicrographs and simulations will be available upon request by any qualified researcher.

Study approval. The study was approved by the institutional ethical committee (approval number 277/13 and 15/19). All subjects gave written informed consent prior to participation.

ACKNOWLEDGEMENTS

The study was supported by a grant of the Interdisciplinary Center of Clinical Research (IZKF) of the Medical Faculty of Würzburg to K.D. and K.G.H (F-N-439). J.L. was supported by a scholarship of the Graduate School of Life Sciences (GSLS) of the University of Würzburg. H.S.H. was supported by the Rudolf-Virchow-Center of the University of Würzburg. L.A. and K.D. hold research fellowships by the Interdisciplinary Center of Clinical Research (IZKF) of the Medical Faculty of Würzburg. We thank Antonia Kohl and Barbara Reuter for excellent technical assistance and A. Balakrishnan and paraphrasis.de for proof-reading. We thank the patients and animals who contributed to the study.

EXTENDED AUTHOR INFORMATION

- Luise Appeltshauser: 0000-0001-5248-4009; LAppeltshauser
- Janis Linke: 0000-0002-4943-4542;
- Hannah S. Heil: 0000-0003-4279-7022; Hannah_SuperRes
- Christine Karus
- Joachim Schenk
- Katherina Hemmen
- Claudia Sommer: 0000-0002-7064-5002;
- Kathrin Doppler: 0000-0003-2883-0009
- Katrin G. Heinze: 0000-0003-2372-6800 @HeinzeLab

AUTHOR CONTRIBUTIONS

K.G.H., K.D., L.A. and H.S.H conceived and designed the experiments. H.S.H. developed the image-correlation analysis routine. J.L. and C.K. performed the sample preparation, imaging and data analysis. J.S. and K.H. performed the image segmentation and analysis of the AiryScan data. K.D. assessed histopathological features. L.A. assessed clinical data and analyzed clinical, histopathological and super resolution microscopy data. L.A., H.S.H, and J.L. wrote the first draft of the manuscript. C.S., K.G.H., and K.D. revised the manuscript for scientific content. All authors read and approved the final manuscript.

COMPETING FINANCIAL INTERESTS

The authors declare no competing financial interests.

medRxiv preprint doi: https://doi.org/10.1101/2022.08.05.22278366; this version posted November 8, 2022. The copyright holder for this preprint (which was not certified by peer review) is the author/funder, who has granted medRxiv a license to display the preprint in perpetuity. It is made available under a CC-BY 4.0 International license .

Bibliography

1. R. Hanewinckel, M.A. Ikram, and P.A. Van Doorn. Peripheral neuropathies. In *Handbook of Clinical Neurology*, volume 138, pages 263–282. Elsevier. ISBN 978-0-12-802973-2. doi: 10.1016/B978-0-12-802973-2.00015-X.
2. Claudia Sommer, Christian Geber, Peter Young, Raimund Forst, Frank Birklein, and Benedikt Schoser. Polyneuropathies. 115(6):83–90. ISSN 1866-0452. doi: 10.3238/arztebl.2018.083.
3. Keiichiro Susuki. Node of ranvier disruption as a cause of neurological diseases. 5(3): AN20130025. ISSN 1759-0914, 1759-0914. doi: 10.1042/AN20130025.
4. Antonino Uncini, Keiichiro Susuki, and Nobuhiro Yuki. Nodo-paranodopathy: Beyond the demyelinating and axonal classification in anti-ganglioside antibody-mediated neuropathies. 124(10):1928–1934. ISSN 13882457. doi: 10.1016/j.clinph.2013.03.025.
5. A. F. Huxley and R. Stämpeli. Evidence for saltatory conduction in peripheral myelinated nerve fibres. 108(3):315–339. ISSN 00223751. doi: 10.1113/jphysiol.1949.sp004335.
6. Matthew N. Rasband and Elior Peles. The nodes of ranvier: Molecular assembly and maintenance. 8(3):a020495. ISSN 1943-0264. doi: 10.1101/cshperspect.a020495.
7. Aniket Ghosh, Diane L. Sherman, and Peter J. Brophy. The axonal cytoskeleton and the assembly of nodes of ranvier. 24(2):104–110. ISSN 1073-8584, 1089-4098. doi: 10.1177/1073858417710897.
8. E. J. Arroyo and S. S. Scherer. On the molecular architecture of myelinated fibers. 113(1): 0001. ISSN 09486143. doi: 10.1007/s00418005000 1.
9. Catherine Faivre-Sarrailh and Jérôme J. Devaux. Neuro-glial interactions at the nodes of ranvier: implication in health and diseases. 7. ISSN 1662-5102. doi: 10.3389/fncel.2013.00196.
10. Konstantin Feinberg, Yael Eshed-Eisenbach, Shahar Frechter, Veronique Amor, Daniela Salomon, Helena Sabanay, Jeffrey L. Dupree, Martin Grumet, Peter J. Brophy, Peter Shrager, and Elior Peles. A glial signal consisting of gliomedin and NrCAM clusters axonal na+ channels during the formation of nodes of ranvier. 65(4):490–502. ISSN 08966273. doi: 10.1016/j.neuron.2010.02.004.
11. Gülsen Çolakoğlu, Ulrika Bergstrom-Tyrberg, Erik O. Berglund, and Barbara Ranscht. Contactin-1 regulates myelination and nodal/paranodal domain organization in the central nervous system. 111(3). ISSN 0027-8424, 1091-6490. doi: 10.1073/pnas.1313769110.
12. Manzoor A. Bhat, Jose C. Rios, Yue Lu, German P. Garcia-Fresco, William Ching, Mary St. Martin, Jingjun Li, Steven Einheber, Mitchell Chesler, Jack Rosenbluth, James L. Salzer, and Hugo J. Bellen. Axon-glia interactions and the domain organization of myelinated axons requires neurexin IV/caspr/paranodin. 30(2):369–383. ISSN 08966273. doi: 10.1016/S0896-6273(01)00294-X.
13. Catherine Faivre-Sarrailh. Molecular organization and function of vertebrate septate-like junctions. 1862(5):183211. ISSN 00052736. doi: 10.1016/j.bbamem.2020.183211.
14. Elisa D'Este, Dirk Kamin, Francisco Balzarotti, and Stefan W. Hell. Ultrastructural anatomy of nodes of ranvier in the peripheral nervous system as revealed by STED microscopy. 114 (2):E191–E199, . ISSN 0027-8424, 1091-6490. doi: 10.1073/pnas.1619553114.
15. Markus Sauer and Mike Heilemann. Single-molecule localization microscopy in eukaryotes. 117(11):7478–7509. ISSN 0009-2665, 1520-6890. doi: 10.1021/acs.chemrev.6b00667.
16. Jörn Heine, Matthias Reuss, Benjamin Harke, Elisa D'Este, Steffen J. Sahl, and Stefan W. Hell. Adaptive-illumination STED nanoscopy. 114(37):9797–9802. ISSN 0027-8424, 1091-6490. doi: 10.1073/pnas.1708304114.
17. Mike Heilemann, Sebastian vandeLinde, Anindita Mukherjee, and Markus Sauer. Super-resolution imaging with small organic fluorophores. 48(37):6903–6908. ISSN 14337851, 15213773. doi: 10.1002/anie.200902073.
18. Christian M. Winterflood, Evgenia Platonova, David Albrecht, and Helge Ewers. Dual-color 3d superresolution microscopy by combined spectral-demixing and biplane imaging. 109 (1):3–6. ISSN 00063495. doi: 10.1016/j.bpj.2015.05.026.
19. Guillaume Jacquemet, Alexandre F. Carisey, Hellyeh Hamidi, Ricardo Henriques, and Christophe Leterrier. The cell biologist's guide to super-resolution microscopy. 133(11). ISSN 0021-9533. doi: 10.1242/jcs.240713.
20. Alistair P. Curd, Joanna Leng, Ruth E. Hughes, Alexa J. Cleasby, Brendan Rogers, Chi H. Trinh, Michelle A. Baird, Yasuharu Takagi, Christian Tiede, Christian Sieben, Suliana Manley, Thomas Schlichthaerle, Ralf Jungmann, Jonas Ries, Hari Shroff, and Michelle Peckham. Nanoscale pattern extraction from relative positions of sparse 3d localizations. 21(3): 1213–1220. ISSN 1530-6984, 1530-6992. doi: 10.1021/acs.nanolett.0c03332.
21. Florian Levet, Guillaume Julien, Rémi Galland, Corey Butler, Anne Beghin, Anaël Chazeau, Philipp Hoess, Jonas Ries, Grégory Giannone, and Jean-Baptiste Sibarita. A tessellation-based colocalization analysis approach for single-molecule localization microscopy. 10(1): 2379. ISSN 2041-1723. doi: 10.1038/s41467-019-10007-4.
22. Christian Werner, Martin Pauli, Sören Doose, Andreas Weishaupt, Holger Haselmann, Benedikt Grünewald, Markus Sauer, Manfred Heckmann, Klaus V. Toyka, Esther Asan, Claudia Sommer, and Christian Geis. Human autoantibodies to amphiphysin induce defective presynaptic vesicle dynamics and composition. 139(2):365–379. ISSN 1460-2156, 0006-8950. doi: 10.1093/brain/awv324.
23. Elisa D'Este, Dirk Kamin, Caroline Velte, Fabian Göttfert, Mikael Simons, and Stefan W. Hell. Subcortical cytoskeleton periodicity throughout the nervous system. 6(1):22741, . ISSN 2045-2322. doi: 10.1038/srep22741.
24. Sven C. Sidenstein, Elisa D'Este, Marvin J. Böhm, Johann G. Danzl, Vladimir N. Belov, and Stefan W. Hell. Multicolour multilevel STED nanoscopy of actin/spectrin organization at synapses. 6(1):26725. ISSN 2045-2322. doi: 10.1038/srep26725.
25. Stéphane Vassilopoulos, Solène Gibaud, Angélique Jimenez, Ghislaine Caillol, and Christophe Leterrier. Ultrastructure of the axonal periodic scaffold reveals a braid-like organization of actin rings. 10(1):5803. ISSN 2041-1723. doi: 10.1038/s41467-019-13835-6.
26. Ke Xu, Guisheng Zhong, and Xiaowei Zhuang. Actin, spectrin, and associated proteins form a periodic cytoskeletal structure in axons. 339(6118):452–456. ISSN 0036-8075, 1095-9203. doi: 10.1126/science.1232251.
27. Claire Yu-Mei Huang, Chuansheng Zhang, Daniel R. Zollinger, Christophe Leterrier, and Matthew N. Rasband. An αII spectrin-based cytoskeleton protects large-diameter myelinated axons from degeneration. 37(47):11323–11334. ISSN 0270-6474, 1529-2401. doi: 10.1523/JNEUROSCI.2113-17.2017.
28. Nicolas Unsain, Martin D. Bordenave, Gaby F. Martinez, Sami Jalil, Catalina von Bilderling, Federico M. Barabas, Luciano A. Masullo, Aaron D. Johnstone, Philip A. Barker, Mariano Bisbal, Fernando D. Stefani, and Alfredo O. Cáceres. Remodeling of the actin/spectrin membrane-associated periodic skeleton, growth cone collapse and f-actin decrease during axonal degeneration. 8(1):3007. ISSN 2045-2322. doi: 10.1038/s41598-018-21232-0.
29. Guisheng Zhong, Jiang He, Ruobo Zhou, Damaris Lorenzo, Hazen P Babcock, Vann Bennett, and Xiaowei Zhuang. Developmental mechanism of the periodic membrane skeleton in axons. 3:e04581. ISSN 2050-084X. doi: 10.7554/eLife.04581.
30. Christophe Leterrier, Pankaj Dubey, and Subhojit Roy. The nano-architecture of the axonal cytoskeleton. 18(12):713–726. ISSN 1471-003X, 1471-0048. doi: 10.1038/nrn.2017.129.
31. I. Horresh, V. Bar, J. L. Kissil, and E. Peles. Organization of myelinated axons by caspr and caspr2 requires the cytoskeletal adapter protein 4.1b. 30(7):2480–2489. ISSN 0270-6474, 1529-2401. doi: 10.1523/JNEUROSCI.5225-09.2010.
32. Y. Ogawa. Spectrins and AnkyrinB constitute a specialized paranodal cytoskeleton. 26(19): 5230–5239. ISSN 0270-6474, 1529-2401. doi: 10.1523/JNEUROSCI.0425-06.2006.
33. Lucas M. P. Chataigner, Christos Gogou, Maurits A. den Boer, Cátia P. Frias, Dominique M. E. Thies-Weesie, Joke C. M. Granneman, Albert J. R. Heck, Dimphna H. Meijer, and Bert J. C. Janssen. Structural insights into the contactin 1 – neurofascin 155 adhesion complex. 13(1):6607. ISSN 2041-1723. doi: 10.1038/s41467-022-34302-9.
34. Kenneth W. Dunn, Malgorzata M. Kamocka, and John H. McDonald. A practical guide to evaluating colocalization in biological microscopy. 300(4):C723–C742. ISSN 0363-6143, 1522-1563. doi: 10.1152/ajpcell.00462.2010.
35. E. M. M. Manders, F. J. Verbeek, and J. A. Aten. Measurement of co-localization of objects in dual-colour confocal images. 169(3):375–382. ISSN 00222720. doi: 10.1111/j.1365-2818.1993.tb03313.x.
36. Menahem Eisenbach, Elena Kartvelishvily, Yael Eshed-Eisenbach, Trent Watkins, Annette Sorensen, Christine Thomson, Barbara Ranscht, Susan C. Barnett, Peter Brophy, and Elior Peles. Differential clustering of caspr by oligodendrocytes and schwann cells. 87(15):3492–3501. ISSN 03604012, 10974547. doi: 10.1002/jnr.22157.
37. Liliana Pedraza, Jeffrey K. Huang, and David Colman. Disposition of axonal caspr with respect to glial cell membranes: Implications for the process of myelination. 87(15):3480–3491. ISSN 03604012, 10974547. doi: 10.1002/jnr.22004.
38. Steven Tait, Frank Gunn-Moore, J. Martin Collinson, Jeffery Huang, Catherine Lubetzki, Liliana Pedraza, Diane L. Sherman, David R. Colman, and Peter J. Brophy. An oligodendrocyte cell adhesion molecule at the site of assembly of the paranodal axo-glial junction. 150(3):657–666. ISSN 0021-9525, 1540-8140. doi: 10.1083/jcb.150.3.657.
39. Jiang He, Ruobo Zhou, Zhuhao Wu, Monica A. Carrasco, Peri T. Kurshan, Jonathan E. Farley, David J. Simon, Guiping Wang, Boran Han, Junjie Hao, Evan Heller, Marc R. Freeman, Kang Shen, Tom Maniatis, Marc Tessier-Lavigne, and Xiaowei Zhuang. Prevalent presence of periodic actin–spectrin-based membrane skeleton in a broad range of neuronal cell types and animal species. 113(21):6029–6034. ISSN 0027-8424, 1091-6490. doi: 10.1073/pnas.1605707113.
40. A. Reles and R. L. Friede. Axonal cytoskeleton at the nodes of ranvier. 20(6):450–458. ISSN 0300-4864, 1573-7381. doi: 10.1007/BF01252273.
41. James L. Salzer. Schwann cell myelination. 7(8):a020529. ISSN 1943-0264. doi: 10.1101/cshperspect.a020529.
42. Tomoko Ishibashi and Hiroko Baba. Paranodal axoglial junctions, an essential component in axonal homeostasis. 10:951809. ISSN 2296-634X. doi: 10.3389/fcell.2022.951809.
43. P. H. Abrahams, A. Day, and G. Allt. The node of ranvier in early wallerian degeneration: A freeze-fracture study. 54(2):95–100. ISSN 0001-6322, 1432-0533. doi: 10.1007/BF00689401.
44. R. H. M. Ballin and P. K. Thomas. Changes at the nodes of ranvier during wallerian degeneration: an electron microscope study. 14(3):237–249. ISSN 0001-6322, 1432-0533. doi: 10.1007/BF00685303.
45. F.L. Mastaglia, W.I. McDonald, and K. Yogendran. Nodal changes during the early stages of wallerian degeneration of central nerve fibres. 30(2):259–267. ISSN 0022510X. doi: 10.1016/0022-510X(76)90132-5.
46. Veronique Amor, Chuansheng Zhang, Anna Vainshtein, Ao Zhang, Daniel R Zollinger, Yael Eshed-Eisenbach, Peter J Brophy, Matthew N Rasband, and Elior Peles. The paranodal cytoskeleton clusters na+ channels at nodes of ranvier. 6:e21392. ISSN 2050-084X. doi: 10.7554/eLife.21392.
47. Chuansheng Zhang, Keiichiro Susuki, Daniel R. Zollinger, Jeffrey L. Dupree, and Matthew N. Rasband. Membrane domain organization of myelinated axons requires βII spectrin. 203(3):437–443. ISSN 1540-8140, 0021-9525. doi: 10.1083/jcb.201308116.
48. Carmen Cifuentes-Diaz, Fabrice Chareyre, Marta Garcia, Jérôme Devaux, Michèle Carnaud, Grégoire Levasseur, Michiko Niwa-Kawakita, Sheila Harroch, Jean-Antoine Girault, Marco Giovannini, and Laurence Goutebroze. Protein 4.1b contributes to the organization of peripheral myelinated axons. 6(9):e25043, . ISSN 1932-6203. doi: 10.1371/journal.pone.0025043.
49. Steven Einheber, Xiaosong Meng, Marina Rubin, Isabel Lam, Narla Mohandas, Xiuli An, Peter Shrager, Joseph Kissil, Patrice Maurel, and James L. Salzer. The 4.1b cytoskeletal protein regulates the domain organization and sheath thickness of myelinated axons. 61(2): 240–253. ISSN 08941491. doi: 10.1002/glia.22430.
50. Kathrin Doppler, Franziska Frank, Ann-Cathrin Koschker, Karlheinz Reiners, and Claudia Sommer. Nodes of ranvier in skin biopsies of patients with diabetes mellitus. 22(3):182–190, . ISSN 10859489. doi: 10.1111/jns.12224.
51. Carmen Cifuentes-Diaz, Odile Dubourg, Theano Irinopoulou, Marc Vigny, Sylvie Lachkar, Laurence Decker, Patrick Charnay, Natalia Denisenko, Thierry Maisonobe, Jean-Marc Léger, Karine Viala, Jean-Jacques Hauw, and Jean-Antoine Girault. Nodes of ranvier and paranodes in chronic acquired neuropathies. 6(1):e14533, . ISSN 1932-6203. doi: 10.1371/journal.pone.0014533.
52. Peter J. Dyck, P. James B. Dyck, and Janean Engelstad. Pathologic alterations of nerves. In *Peripheral Neuropathy*, pages 733–829. Elsevier. ISBN 978-0-7216-9491-7. doi: 10.1016/B978-0-7216-9491-7.50035-1.
53. Claudia Sommer. Nerve and skin biopsy in neuropathies. 31(5):534–540. ISSN 1350-7540,

medRxiv preprint doi: https://doi.org/10.1101/2022.08.05.22278366; this version posted November 8, 2022. The copyright holder for this preprint (which was not certified by peer review) is the author/funder, who has granted medRxiv a license to display the preprint in perpetuity. It is made available under a CC-BY 4.0 International license .

1473-6551. doi: 10.1097/WCO.0000000000000601.

54. Joachim Weis, Sebastian Brandner, Martin Lammens, Claudia Sommer, and Jean-Michel Vallat. Processing of nerve biopsies: A practical guide for neuropathologists. 31(1):7–23. ISSN 0722-5091. doi: 10.5414/NP300468.
55. Jean-Michel Vallat, Anne Vital, Laurent Magy, Marie-Laure Martin-Negrier, and Claude Vital. An update on nerve biopsy. 68(8):833–844. ISSN 0022-3069, 1554-6578. doi: 10.1097/NEN.0b013e3181af2b9c.
56. Beate Hartmannsberger, Kathrin Doppler, Julia Stauber, Beate Schlotter-Weigel, Peter Young, Michael W Sereda, and Claudia Sommer. Intraepidermal nerve fibre density as biomarker in charcot–marie–tooth disease type 1a. 2(1):fcaa012. ISSN 2632-1297. doi: 10.1093/braincomms/fcaa012.
57. J. Michael Schröder. Developmental and pathological changes at the node and paranode in human sural nerves. 34(5):422–435. ISSN 1059-910X, 1097-0029. doi: 10.1002/(SICI)1097-0029(19960801)34:5<422::AID-JEMT2>3.0.CO;2-O.
58. Kathrin Doppler, Luise Appeltshauser, Heidrun H. Krämer, Judy King Man Ng, Edgar Meinl, Carmen Villmann, Peter Brophy, Sulayman D. Dib-Hajj, Stephen G. Waxman, Andreas Weishaupt, and Claudia Sommer. Contactin-1 and neurofascin-155/-186 are not targets of auto-antibodies in multifocal motor neuropathy. 10(7):e0134274, . ISSN 1932-6203. doi: 10.1371/journal.pone.0134274.
59. Varun Venkataramani, Frank Herrmannsdörfer, Mike Heilemann, and Thomas Kuner. SuReSim: simulating localization microscopy experiments from ground truth models. 13 (4):319–321. ISSN 1548-7091, 1548-7105. doi: 10.1038/nmeth.3775.
60. Martin Ovesný, Pavel Křížek, Josef Borkovec, Zdeněk Švindrych, and Guy M. Hagen. ThunderSTORM: a comprehensive ImageJ plug-in for PALM and STORM data analysis and super-resolution imaging. 30(16):2389–2390. ISSN 1367-4803, 1460-2059. doi: 10.1093/bioinformatics/btu202.
61. M.D. Abramoff, Paulo J. Magalhães, and Sunanda J. Ram. Image processing with ImageJ. 11(7):36–42. ISSN 1081-8693.
62. Ignacio Arganda-Carreras, Carlos O. S. Sorzano, Roberto Marabini, José María Carazo, Carlos Ortiz-de Solorzano, and Jan Kybic. Consistent and elastic registration of histological sections using vector-spline regularization. In Reinhard R. Beichel and Milan Sonka, editors, *Computer Vision Approaches to Medical Image Analysis*, volume 4241, pages 85–95. Springer Berlin Heidelberg. ISBN 978-3-540-46257-6 978-3-540-46258-3. doi: 10.1007/11889762_8. Series Title: Lecture Notes in Computer Science.
63. Dirk Padfield. Generalized normalized cross correlation.
64. Johannes Schindelin, Ignacio Arganda-Carreras, Erwin Frise, Verena Kaynig, Mark Longair, Tobias Pietzsch, Stephan Preibisch, Curtis Rueden, Stephan Saalfeld, Benjamin Schmid, Jean-Yves Tinevez, Daniel James White, Volker Hartenstein, Kevin Eliceiri, Pavel Tomancak, and Albert Cardona. Fiji: an open-source platform for biological-image analysis. 9(7): 676–682. ISSN 1548-7091, 1548-7105. doi: 10.1038/nmeth.2019.
65. Diane L. Sherman, Steven Tait, Shona Melrose, Richard Johnson, Barbara Zonta, Felipe A. Court, Wendy B. Macklin, Stephen Meek, Andrew J.H. Smith, David F. Cottrell, and Peter J. Brophy. Neurofascins are required to establish axonal domains for saltatory conduction. 48 (5):737–742. ISSN 08966273. doi: 10.1016/j.neuron.2005.10.019.
66. Barbara Zonta, Steven Tait, Shona Melrose, Heather Anderson, Sheila Harroch, Jennifer Higginson, Diane L. Sherman, and Peter J. Brophy. Glial and neuronal isoforms of neurofascin have distinct roles in the assembly of nodes of ranvier in the central nervous system. 181(7):1169–1177. ISSN 1540-8140, 0021-9525. doi: 10.1083/jcb.200712154.

Online Methods

Patients, clinical and histopathological diagnosis. We prospectively included n = 17 patients with peripheral neuropathies who had undergone a sensory nerve biopsy during the routine diagnostic workup process at the University hospital of Würzburg between July 2018 and April 2021. Clinical and histopathological data were assessed as described in the Supporting Note 1 and are shown in Supporting Table S1 and S2. The study was performed in line with the principles of the Declaration of Helsinki and was approved by the institutional ethical committee (approval number 277/13 and 15/19). All subjects gave written informed consent prior to participation.

Teased fiber preparation. Murine teased fibers we prepared as previously described (58). In brief, adult C57/Bl6 mice were sacrificed by cervical dislocation. Sciatic and sural nerve were dissected, fixed for 10 minutes in 4% PFA, and washed in 1M phosphate buffer. Human sensory nerve preparations (n = 16 sural nerve, n = 1 superficial radial nerve) were obtained from leftovers of routine nerve biopsies of patients with polyneuropathies undergoing a diagnostic workup process at the University Hospital of Würzburg. The nerve was cut into 5-mm slices with a scalpel, fixed and washed as described above. Epineural connective tissue and the perineurium were removed with fine forceps. The remaining nerve fascicle was including endoneurial connective tissue was teased with fine forceps in 0.5M phosphate buffer, so that single axons and /or bundles were separated. For *d*STORM microscopy, the fibers were teased on ultra-cleaned, PDL-coated 24-mm glass coverslips. For confocal microscopy, the fibers were teased on Airyscan Superfrost Slides. Slides and coverslips were dried overnight and stored at -20°C until use. The teasing process was performed by a technician or investigator and two or less attempts on learning the teasing process resulted in sufficient results. The whole procedure of human sural nerve fixation, preparation and teasing took a maximum of 60 minutes or less.

Simulated Datasets. Simulations of super-resolution microscopy datasets were performed with the SuReSim software package (59). The periodic ground truth structure is available on Zenodo (see data sharing statement) and the simulation parameters are summarized in Supplemental Table S6). The localization text-files were transformed into ThunderSTORM (60) compatible csv-files and super-resolution images with a custom MatLab script. Simulated datasets were analyzed the same way as the experimental datasets (see below).

Immunostaining for *d*STORM and confocal microscopy. The thawed teased fibers were fixed for 20 minutes in 100% Acetone at -20 °C. After washing with Phosphate-buffered saline (PBS) and permeabilization with 2% Triton-X for 30 min, they were blocked in PBS containing 1mg/ml Biotin-BSA, 4% BSA and 0,5% Triton-X for 60 min. Dual-color immunolabeling was performed by overnight incubation at + 4 °C with the primary antibody diluted in PBS with 0.5% Triton-X and 1% BSA (see Supplemental Table S7). For *d*STORM imaging, fiducial markers were immobilized on the surface by an additional 20 min incubation step with 0.1 mg/ml Neutravidin (Thermo Scientific™, 31000) and three PBS washing steps right before the initiation of the secondary antibody incubation. During the secondary antibody incubation 35 pM biotinylated gold nanorods (Nanopartz C12-25-650-TB) were added. After secondary antibody incubation for 1h at room temperature, slides and coverslips were washed and *d*STORM coverslips were stored PBS. For Airyscan imaging, the slides were embedded in Vectashield antifade mounting medium (Vector laboratories, VEC-H-1000).

***d*STORM Fluorescence image acquisition.** Dual-color *d*STORM microscopy was performed with an inverted light microscope (Zeiss Observer Z.1, Carl Zeiss AG) customized for SMLM (Supplemental Table S8). The *d*STORM blinking buffer contained 100 mM MEA (Sigma, M6500), 20 mM D-glucose (Sigma, G7528), 0.55 mg ml-1 gluco-oxidase (Roth, 60281), 0.011 mg ml-1 catalase (Sigma, C1345) in PBS. The pH was adjusted to pH 7.9 with 5M KOH (Sigma, 30603). After applying the *d*STORM buffer, imaging was performed

medRxiv preprint doi: https://doi.org/10.1101/2022.08.05.22278366; this version posted November 8, 2022. The copyright holder for this preprint (which was not certified by peer review) is the author/funder, who has granted medRxiv a license to display the preprint in perpetuity. It is made available under a CC-BY 4.0 International license .

with the acquisition parameters summarized in Supplemental Table S9. For color channel alignment, calibration images with 100 nm TetraSpeck microspheres (ThermoFisher, T7279) immobilized on glass coverslips were recorded simultaneously in both channels.

***d*STORM image reconstruction.** *d*STORM images were reconstructed with the ImageJ plugin ThunderSTORM (60, 61) as specified in Supplemental Table S9). Based on the filtered localization data, a super-resolved image with a pixel size of 10.6 nm was reconstructed by Gaussian rendering or as a scatter plot. For the channel alignment, the TetraSpeck images were localized and a super-resolved image with a pixel size of 10.6 nm was reconstructed for each channel. Based on these calibration images, a transformation matrix of the A532 channel onto the A647 was calculated with the ImageJ plugin bunwarpJ (62). This transformation matrix was directly applied to the reconstructed super-resolved images or to the localization data itself with a MatLab script.

***d*STORM image autocorrelation analysis.** The image autocorrelation analysis was performed based on the localization data with a MatLab routine (Scripts and manuals are available on Zenodo, see Data sharing statement). With the routine, several regions of interest (ROIs) within the paranodal and internodal region were selected manually in the super-resolved reconstruction of the respective node (width = 600 nm; lengths along the axon were manually chosen by selecting a start and end point of the centerline). Based on localization data contained in each ROI, a super-resolved image was reconstructed after rotating the ROI to align the image along the x-axis. The rotation angle was varied within a ± 20° range by 1°- steps to align the repetitive line structure perpendicularly to the x-axis. The resulting reconstructed images were autocorrelated in 2D with the Normxcorr2_general.m function (63). The optimal rotation angle was selected based on a maximizing of the autocorrelation along the center y-axis. MatLab output correlation images (pixelsize 2 nm) were analyzed in FIJI (64) with line plots averaged over a width of 150 pixels. Plots were imported into OriginPro (Origin2021b, OriginLab Corp.). Gauss distribution curves were fitted and the peak to peak distances of those distribution curves were calculated.

***d*STORM image colocalization analysis.** To estimate the image resolution the raw time series image stacks were split into even and colocalization analysis on transformed dual-color *d*STORM datasets was performed with a tessellation-based approach (21). Paranodal regions were defined by Caspr-1 staining, each representing a region of interest. Herewithin, Manders' A & B correlation coefficients of all channels were calculated to assess colocalization (34, 35). The pan-neurofascin antibody used in this study stained both glial neurofascin-155 isoform at the paranode and neuronal neurofascin-186 isoform at the node, which have different localizations and functions (65, 66). In this study, we exclusively studied neurofascin-155 and its interaction with Caspr-1, therefore we exclusively studied the paranodal region. The nodal region within the pan-neurofascin staining was not considered in the analysis. The colocalization data was analyzed using OriginPro.

Large field of view confocal imaging and assessment. High-content 3D three-color confocal microscopy at a 20-fold magnification including stacks and tiles was performed with a Zeiss LSM 980 with Airyscan 2 (Carl Zeiss AG) using Zen blue 3.3 software (Carl Zeiss AG) for Airyscan 3D processing and stitching of tiles. Acquisition and image processing parameters are listed in Supporting Table S9. To count and locate nodes of Ranvier within the sample and to determine the node of Ranvier density within the sample, we performed and compared either manual counting combined with background segmentation using FIJI, semi-automated threshold-based segmentation considering specific anti-pan-neurofascin staining using Imaris software (v.9.9.0, Oxford instruments, Abingdon, UK) or fully automated image segmentation using deep learning (see Supporting Notes 2 and 3). To assess normal values for nodo-paranodal morphometrics, we measured n = 69 morphologically intact human nodes of Ranvier from n = 4 patients of our cohort with mild neuropathy and only minor pathological alterations in the semithin sections (see Supporting Table S5). Healthy nodes were identified by 1) two opposing and symmetric Caspr-1 blocks, 2) homogeneous staining and 3) rectangular form. A blinded investigator performed manual measurements by defining linear ROIs using FIJI. We assessed 1) the maximal extension of two opposing Caspr-1 blocks including the nodal gap as an indicator of nodo-paranodal length, 2) the minimal gap between two Caspr-1 blocks as an indicator of the nodal length and 3) the maximal Caspr-1 diameter as an indicator of the paranodal axonal diameter (see Figure 5 A-B and the Movie M1). N = 40 randomly selected nodes of Ranvier were measured in each patient sample of n = 9 patients. In n = 7 patients, the maximal number of nodes per field of view was < 40 nodes, so all visible nodes within the field of view were assessed (n = 22 - 39 nodes, see S5). The manual analysis was compared to automated measurements of nodo-paranodal length. Accuracy of deep learning or threshold based image segmentation did not reach as exact results as manual measurement (see Supporting Note 3 and Supporting Fig. S4).

Statistics. We assessed statistical significance with OriginPro Version 2021b SR2 9.8.5.212 (OriginLab Corp.) and Prism V9.3.0 (GraphPad Software, San Diego, CA). Testing for normality distribution was performed using d'Agostino Pearson test and Shapiro-Wilk test. The further specific tests used in the analysis are described in the respective figure and table legends. Results with p-values less than 0.05 were considered significant.

medRxiv preprint doi: https://doi.org/10.1101/2022.08.05.22278366; this version posted November 8, 2022. The copyright holder for this preprint (which was not certified by peer review) is the author/funder, who has granted medRxiv a license to display the preprint in perpetuity. It is made available under a CC-BY 4.0 International license .

Super-resolution imaging pinpoints ultrastructural changes at the node of Ranvier in patients with polyneuropathy

Appeltshauser, Linke & Heil et al., 2022

Supplementary Material

Supplorting Notes 1-5.

Supplementary Tables 1-9.

Supplementary Figures 1-4.

Supplementary Movie 1.

Supplementary Bibliography.

medRxiv preprint doi: https://doi.org/10.1101/2022.08.05.22278366; this version posted November 8, 2022. The copyright holder for this preprint (which was not certified by peer review) is the author/funder, who has granted medRxiv a license to display the preprint in perpetuity. It is made available under a CC-BY 4.0 International license .

Supporting Notes

Supplementary Note 1: Assessment of patients' clinical and histopathological data

Demographic and clinical data of the n = 17 patients including laboratory results, nerve conduction studies and suspected clinical diagnosis were assessed retrospectively from the patients' records. HbA1c values were assessed at the time point of the nerve biopsy and diabetes mellitus was classified according to WHO criteria. Diagnostic criteria for chronic inflammatory demyelinating polyradiculoneuropathy (CIDP) (1), POEMS syndrome (2) and vasculitic neuropathy (3) were assessed in patients with the respective clinical diagnosis. Clinical disease severity respective to motor function was assessed retrospectively by applying standardized clinical scores: The Overall disability sum Score (ODSS) (4) and the Medical Research Council (MRC) Sum Score for levels of paresis (5). The histopathological diagnosis was assessed in each biopsy by a trained and blinded researcher reevaluating the routine staining including semithin sections with toluidine blue staining, cryosection including H&E staining and immunohistochemistry for T-cell marker anti-CD4 and paraffin-embedded sections including H&E, Congo red and Elastica van Gieson staining and immunohistochemistry for macrophages using anti-CD68 and lymphocytes using anti-CD8 according to standard protocols as previously described (6). Onion bulb structures, regeneration clusters, thinly myelinated fibers and Wallerian degeneration were counted per fascicle in each patient. Axonal loss was quantified in a semi-quantitative manner (mild, moderate, severe) and large fibers per fascicle were counted and the area of the fascicle was measured using FIJI (7, 8) to calculate the fiber density (unit: fibers/mm^2).

Supplementary Note 2: Implementation of automated image analysis methods and deep learning strategies to assess nodes of Ranvier in teased fiber preparations

A. Threshold based segmentation. To count and locate nodes of Ranvier, we performed semi-automated threshold based image segmentation of the specific anti-pan-neurofascin staining using Imaris (v9.9.0, Oxford instruments, Abingdon, UK). Imaging smoothing was set to 2 times pixelsize (0.15 µm). The intensity threshold was set manually to values between 500 - 1400 to include stained nodes of Ranvier individually for every image. Results were filtered by object size (5000 voxel). Analysis was performed in n = 20 high-content images of murine sciatic nerves and human samples each. For comparison and accuracy assessment, the number of nodes per sample was counted manually using FIJI by two independent and blinded investigators. To determine the node of Ranvier density within the sample, the total tissue volume was calculated based on unspecific background binding of the anti-pan-neurofascin antibody using a custom FIJI script (available on Zenodo, see data sharing statement). Images were filtered with a 3D Gaussian blur and then classified into "tissue" and "non tissue" by a low static threshold. Morphometrics of the nodes of Ranvier were assessed and compared via two methods: Firstly, nodo-paranodal length was calculated from Imaris ellipsoid axes of pan-neurofascin staining in n = 20 slides of murine and human samples (see above and Supporting Fig. S4). Secondly, morphometrics were assessed on the same slides in a blinded manner by FIJI defining linear ROIs as indicated in Figure 5.

B. Automated image segmentation using deep learning. Fully automated image segmentation of specific anti-pan-neurofascin stained nodes of Ranvier with an artificial neural network was performed using custom python scripts utilizing ResNet-101 retrieved from the Pytorch library (9, 10). First, individual z-slices of high content images were split into smaller tiles (224*224 px) and individually downscaled with a min/max scaling. Image tiles were then converted to RGB and transformed with the network's default transformation functions. Training for patient high content image segmentation was performed using 40 randomly selected image slices and 100.000 training iterations with batches of 50 tiles per iteration. Loss was calculated via cross entropy, weights were optimized using the Adam optimizer and a learning rate of 1e-6. To minimize network habituation to the training data, three layers of randomization were used for every iteration: A random image was opened, the seed point for tile creation was randomized and the tiles included in the batch were randomly chosen. The final prediction of the pixel classification was calculated twice with different seed points for tile creation. Only pixel detected in both classifications were included to minimize tile border effects. Analysis of the pixel classification data was performed using the skimage image library. Objects were labeled and object statistics (area, position, axis length, intensities of the original image) were calculated with skimage built-in functions on a max-projection.

Supplementary Note 3: Implementing deep learning strategies and automated image analysis methods on teased fiber assessment

To achieve accurate, unbiased counting and morphometrics and to seek ways to enhance diagnostic assessment of nerve biopsies in the future, we implemented automated image analysis methods on large field-of-view photomicrographs of teased fiber preparations (see above and Supporting Fig. S4 A-C). Counting accuracy of the node of Ranvier density was compared to manual assessment. As a result, deep learning (DL) based median counting accuracy in murine datasets was 0.99 (0.75 - 1.15) and 1.21 (0.09 - 4.43) in human datasets. The semi-automated, segmentation-based approach failed toreach the same accuracy,

medRxiv preprint doi: https://doi.org/10.1101/2022.08.05.22278366; this version posted November 8, 2022. The copyright holder for this preprint (which was not certified by peer review) is the author/funder, who has granted medRxiv a license to display the preprint in perpetuity. It is made available under a CC-BY 4.0 International license .

with a median of 1.21 (0.97 - 2.42) for murine datasets and 2.83 (0.38 - 10.0) in human datasets, with significant differences compared to the DL based strategy (see Supporting Fig. S4 D). The nodal count correlated between manual assessment and DL based assessment when compared in single samples both for murine and human datasets (Spearman $r = 0.91$, $p < 0.0001$ and $r = 0.87$, $p < 0.0001$). Recognition using segmentation had a reduced counting accuracy with a significantly increased variance (mouse: $F = 0.033$, $p < 0.05$ human: $F = 0.033$, $p < 0.0001$), possibly due to the heterogeneity of pathological alterations. Thus, we could show that DL based routines can accurately count nodes of Ranvier in teased fiber bundles in a fully automated manner, and are superior to segmentation-based approaches. Furthermore, we seeked to implement automated morphometrical analysis including assessment of nodo-paranodal length via DL and threshold based approaches. Therefore, we assessed nodo-paranodal length from the object statistics, which were extracted from the detected nodes of Ranvier by DL and threshold based image segmentation, and compared them to the manually assessed measurements as described above. In both DL and threshold based analysis, the results differed significantly between automated and manual analysis both in murine samples (median nodo-paranodal length by manual assessment: 8.6 ± 1.5 vs. DL based measurement 7.2 ± 2.7 $p = 0.02$, vs. threshold based measurement 6.9 ± 4.2 $p < 0.0001$) and in human samples (median nodo-paranodal length per manual assessment: 10.9 ± 7.0 vs. DL based measurement 7.8 ± 4.2 $p < 0.001$, vs. threshold based measurement 6.1 ± 31.0 $p < 0.0001$). Thus, automated image analysis did not yet reach the same accuracy as manual measurement by two blinded, independent investigators, especially in pathologically altered samples (see Supporting Fig. S4E). In conclusion, we can thus show that deep learning based assessment can add to the diagnostic assessment of teased fiber analysis. In previous studies, segmentation techniques and deep learning algorithms have not only been applied on super resolution data, but also on rodent and porcine peripheral nerve and human healthy CNS cross sections (11–15). Most recently, super resolution microscopy and image segmentation was successfully implemented on healthy human peripheral nerve cross sections (16). Our data provide a new application for these new techniques. Better training sets and new DL algorithms may also allow for DL to be used for morphometric assessment in the future, and thus enhance diagnostic means. As an outlook, the DL based methodology introduced in this study paves the way to navigate within a sample and to establish automated target recognition in large and dense samples, with following dSTORM imaging of regions of interest. Thereby, nanoscale pathology could be assessed in a fully automated manner, and thus be translated to routine diagnostics. Future studies need to address and further investigate these new approaches.

Supplementary Note 4: Supporting Note S2: Morphometric analysis of patients' teased fiber preparations using high-content confocal imaging

We assessed nodo-paranodal length, paranodal diameter and nodal length as described in detail in the methods in the main manuscript. Results on nodo-paranodal length are described in detail in the main manuscript. The nodal length did not differ between patient cohorts with acute, chronic axonal and demyelinating neuropathy compared to intact nodes, nor between patient cohorts with mild, moderate or severe axonal loss (see Table 1). Still, we found significant nodal elongations in single patients who were clinically severely affected (see Supporting Table S3). In the whole cohort, the nodal length correlated to clinical motor function scores (mean nodal length vs. Overall disability sum score: Pearson $r = 0.59$, $p = 0.01$; mean nodal length vs. Medical Research Council Sum Score: Pearson $r = -0.83$, $p < 0.0001$), but not to histopathological severity of axonal loss. Most patients with axonal neuropathies showed normal paranodal axonal diameters (see Table 1 and Supporting Table S5). On the other hand, the paranodal diameter in patients with chronic demyelinating polyneuropathy was 2.7 µm and thus significantly increased compared to intact nodes, and compared to patients with acute and chronic axonal neuropathy ($p < 0.0001$). Thus, paranodal swelling was found to be prominent in patients with demyelinating neuropathies. We did not detect any correlation of clinical or histopathological disease severity and axonal diameter. In all analyses, age was considered as a possible confounder, but did not correlate to any of the measured parameters. In conclusion, the morphometric data on nodal length and diameter help to discriminate single patients regarding clinical disease severity and type of neuropathy. Despite a small sample size, we identify paranodal swelling as exclusive for demyelinating disease, as previously described in avian models of demyelination and in patients with multiple sclerosis (17, 18). Furthermore, we find nodal elongation in single patients as a possible indicator of clinically severe demyelinating disease, corresponding to previous reports on nodal elongations in patients with in CIDP (19). Thus, these parameters may be valuable in histopathological diagnostic assessment of patients with neuropathies of unknown etiology, but need to be validated in larger studies with homogenous cohorts. As a limitation, we cannot address yet to what extent internodal and nodo-paranodal changes are physiological and occur with age in the elderly due to a lack of human healthy controls due to ethical reasons, as post-mortem autopsy material as a control might not be suited due to immediate and early post-mortem cytoskeletal and structural alterations (20). Still, we did not observe a correlation of age to nodo-paranodal parameters, arguing against age being a confounder in the analysis.

medRxiv preprint doi: https://doi.org/10.1101/2022.08.05.22278366; this version posted November 8, 2022. The copyright holder for this preprint (which was not certified by peer review) is the author/funder, who has granted medRxiv a license to display the preprint in perpetuity. It is made available under a CC-BY 4.0 International license .

Supplementary Note 5: Paranodal detachment in axonal neuropathy differs from autoimmune nodo-paranodopathy and demyelinating neuropathy

The pathomechanism of nodo-paranodal disruption in axonal neuropathies we propose within this study is different to previously suggested mechanisms of nodo–paranododal disruption in autoantibody-mediated nodo-paranodopathy. This rare disease is an autoimmune neuropathy associated with pathogenic autoantibodies against proteins located at the node of Ranvier, which attack proteins of the axoglial junction. As a consequence, a primary axoglial detachment induced by the autoantibodies has been proposed, either by directly inhibiting the interaction of axonal and glial binding partners or by altered myelin turnover (21–25). Due to its characteristic clinical and pathophysiological features, autoimmune neuropathy has been proposed as a new sub-entity within immune-mediated neuropathies (1, 26). However, our cohort does not include patients with this rare disease, as today, antibodies serve as a biomarker and reduce the need for invasive diagnostic procedures. Additionally, nodal elongations measured by the gap of myelin basic protein have also been described in skin biopsies of patients with chronic inflammatory demyelinating neuropathy (19, 27, 28). In this study, we found paranodal elongations measured by Caspr-1 staining in patients with acute axonal neuropathy to be significantly longer than in CIDP. Still, our CIDP cohort is small and not typical, as diagnosis of CIDP usually does not need nerve biopsy and is only performed in unclear cases. We thus cannot directly compare these possible mechanisms of axoglial disjunction. Still, we hypothesize that in axonal neuropathies, the axoglial complex remains intact, but detaches from its cytoskeletal anchor, whereas autoimmune nodopathies lead to a axoglial detachment (24, 25, 29–31). The methods described in this study yield the opportunity to investigate and directly compare different mechanisms of paranodal damage on a nanostructural scale in future studies, e.g. including cell-culture-based assays.

medRxiv preprint doi: https://doi.org/10.1101/2022.08.05.22278366; this version posted November 8, 2022. The copyright holder for this preprint (which was not certified by peer review) is the author/funder, who has granted medRxiv a license to display the preprint in perpetuity. It is made available under a CC-BY 4.0 International license .

Supplementary Tables

no	age	sex	clinical presentation	NCS classification	SNAP (µV)	SNAP (% of LLN)	disease duration (months)	diabetes mellitus	HbA1c	CSF (cells; total protein in mg/l)	suspected etiology	diagnostic criteria (EAN/PNS (1, 3))
1	21-30	male	distal asymmetric sensorimotor	axonal	4.7	47	18	no	5.3	n/a	vasculitic	pathologically definite vasculitic neuropathy(3)
2	61-70	male	distal asymmetric sensorimotor	axonal	7.0	70	12	no	6.0	1/497	vasculitic	clinically probable vasculitic neuropathy(3)
3	81-90	male	distal symmetric sensorimotor	axonal	0.0	0	2	no	6.5	n/a	vasculitic	pathologically definite vasculitic neuropathy(3)
4	51-60	male	distal asymmetric sensorimotor	axonal	0.0	0	7	no	5.1	2/404	vasculitic	clinically probable vasculitic neuropathy(3)
5	61-70	male	distal asymmetric sensorimotor	axonal	1.8	36	1	no	5.8	1/396	vasculitic	clinically probable vasculitic neuropathy(3)
6	71-80	female	distal symmetric sensorimotor	axonal	0.0	0	5	yes	6.3	3/1070	POEMS	POEMS(2)
7	51-60	female	distal asymmetric sensorimotor	axonal	2.1	70	15	yes	6.5	3/606	vasculitic	clinically probable vasculitic neuropathy(3)
8	71-80	male	distal symmetric sensorimotor	axonal	0.0	0	1	no	5.5	3/796	vasculitic	clinically probable vasculitic neuropathy(3)
9	31-40	male	distal symmetric sensorimotor	demyelinating	7.7	77	96	no	5.9	3/333	unknown/ vitamin B12 deficiency	n/a
10	61-70	female	distal symmtric sensorimotor	axonal	2.7	54	20	no	5.7	1/454	unknown	n/a
11	61-70	male	proximal asymmetric sensorimotor	axonal	1.9	38	55	no	5.7	4/407	unknown	n/a
12	51-60	male	distal symmetric sensorimotor	demyelinating	10.5	100	4	no	4.9	28/2700	CIDP variant	CIDP(1)
13	51-60	male	distal symmetric sensorimotor	mixed	2.9	29	26	no	5.0	2/586	CIDP	possible CIDP(1)
14	31-40	male	distal symmetric sensorimotor	demyelinating	3.4	34	264	no	5.1	4/1940	CIDP	CIDP(1)
15	61-70	male	distal asymmetric sensorimotor	mixed	5.2	52	69	no	5.4	5/618	CIDP variant	possible CIDP(1)
16	51-60	female	distal asymmetric sensorimotor	axonal	7.0	70	21	no	n/a	2/211	CIDP variant	possible CIDP(1)
17	61-70	male	distal symmetric sensorimotor	axonal	0.0	0	243	no	5.3	1/599	hereditary	n/a

Table S1. Demographic data and clinical of the cohort of patients with polyneuropathy. Abbreviations: CIDP = chronic inflammatory demyelinating polyradiculoneuropathy, CSF = cerebrospinal fluid, n/a = not applicable or not assessed, LLN = lower limit of normal, NCS = nerve conduction studies, no = number, POEMS = polyneuropathy, organomegaly, endocrinopathy, myeloma protein, and skin changes (osteosclerotic myeloma), SNAP = Sensory nerve action potential.

medRxiv preprint doi: https://doi.org/10.1101/2022.08.05.22278366; this version posted November 8, 2022. The copyright holder for this preprint (which was not certified by peer review) is the author/funder, who has granted medRxiv a license to display the preprint in perpetuity. It is made available under a CC-BY 4.0 International license .

no	onion bulbs	regenerating clusters	thinly myelinated fibers	Wallerian degeneration	large fibers	fascicle area (μm^2)	fiber density (large fibers/mm^2)	mean fiber density	signs of inflammation/vessel pathology	severity axonal loss	acuteness	type
1	0/0	0/0	2/2	2/1	297/129	131469/114096	2259/1131	1695	perivascular leukocytes (including the vessel wall), fragmentation of lamina elastica interna, necrosis	moderate	acute	axonal
2	0/0	2/1	3/0	4/5	222/132	118621/68965	1872/1914	1893	perivascular leukocytes (including the vessel wall)	moderate	acute	axonal
3	0/0	0/2	0/0	16/6	50/141	130332/117842	384/1197	790	perivascular leukocytes (including the vessel wall), fragmentation of internal elastic lamina	moderate	acute	axonal
4	0/0	2/0	0/0	9/6	10/11	114664 / 98878	87 / 111	99	perivascular leukocytes (including the vessel wall), endoneural macrophages	severe	acute	axonal
5	0/0	0/0	0/0	32/42	32/42	103204/72460	230/745	488	perivascular leukocytes (including the vessel wall), endoneural macrophages	severe	acute	axonal
6	0/0	4/0	4/2	3/11	38/29	105348/54121	361/546	453	perivascular leukocytes	severe	acute	axonal
7	0/0	2/2	3/1	0/2	67/410	57923/107453	1157/3816	2486	perivascular leukocytes, endoneural macrophages	mild	chronic	axonal
8	5/1	9/6	4/1	0/0	71/161	58634/103384	1211/1557	1384	perivascular leukocytes, fragmentation of elastic lamina	moderate	chronic	axonal
9	3/3	3/2	3/3	0/0	121/98	113839/55362	1063/1770	1417	none	moderate	chronic	axonal
10	0/0	7/5	18/12	0/0	185/143	85716/51282	2158/2788	2473	none	moderate	chronic	axonal
11	0/0	3/4	4/2	3/3	191/134	62462/42427	3058/3158	3108	endoneural macrophages	mild	chronic	axonal
12	3/0	8/5	5/2	0/0	552/218	104192/75243	5298/2897	4098	perineural leukocytes	mild	chronic	axonal
13	5/0	2/0	35/3	2/1	98/24	66966/19482	1463/1232	1348	perivascular leukocytes, perivascular and endoneural macrophages	severe	chronic	demyelinating
14	3/6	7/6	18/3	0/0	205/196	104881/115955	1955/1690	1822	endoneural and perivascular leukocytes, endoneural macrophages	moderate	chronic	demyelinating
15	2/1	4/6	29/41	0/1	125/142	52967/194474	2360/1359	1860	none	moderate	chronic	demyelinating
16	2/2	0/1	12/7	0/1	215/155	87379/54731	2461/2832	2646	endoneural and perivascular macrophages	mild	chronic	demyelinating
17	2	6/2	24/6	0/0	110/95	78121/55787	1408/1703	1555	none	moderate	chronic	demyelinating

Table S2. Histopathologic parameters and classification of patients with polyneuropathy. In each patient, semithin cross sections of sensory nerve biopsy (patient 7: superficial radial nerve, other patients: sural nerve) with toluidine blue staining were evaluated for histopathological classification. Total counts of onion bulb figures, thinly myelinated fibers, Wallerian degeneration and large fibers are displayed for two fascicles per patient. Fascicle area was measured using FIJI. Fiber density was calculated as n(large fibers) / mm^3 and is displayed both for the single fascicles and as the mean fiber density. Furthermore, immunostainings were evaluated as described in the methods to check for signs of inflammation and amyloid deposition, and if positive, are reported above. Histopathologic classification including semiquantitative assessment of axonal loss, acuteness of disease and type (axonal or demyelinating) was performed by a trained and blinded researcher. Abbreviations: no = number.

medRxiv preprint doi: https://doi.org/10.1101/2022.08.05.22278366; this version posted November 8, 2022. The copyright holder for this preprint (which was not certified by peer review) is the author/funder, who has granted medRxiv a license to display the preprint in perpetuity. It is made available under a CC-BY 4.0 International license .

3A) type	**axonal** (n=12)	**demyelinating** (n=5)	**p-value**
median count of onion bulbs/fascicle	0	2	0.0047
median count of thinly myelinated fibers/fascicle	2.3	15	0.0015
3B) acuteness	**acute** (n=6)	**chronic** (n=12)	**p-value**
median Wallerian degeneration figures/fascicle	7.3	0.0	0.0003
median count of regenerating clusters / fascicle	1.0	4.0	0.0076
median disease duration (months)	6	42	0.021

3C) severity	**mild** (n=4)	**moderate** (n=8)	**sever** (n=4)	**p-value**
mean large fiber density (1/mm^2)	3085 ± 725	1654 ± 459	597 ± 531	$p_{mild\,vs.\,sever} < 0.0001$ $p_{moderate\,vs.\,sever} = 0.0176$
SNAP (% of LLN)	69.6 ± 25.32	37.11 ± 30.54	16.25 ± 18.98	$p_{mild\,vs.\,sever} < 0.04$ $p_{moderate\,vs.\,sever} = 0.4$

Table S3. Histopathological and clinical differences between groups of histopathological classification. For histopathological classification, patients were classified into histopathological 3A) type (axonal and demyelinating neuropathy) by counting signs of demyelination such as onion bulb figures and thinly myelinated fibers/fascicle. Furthermore, 3B) histopathological acuity was determined by counting signs of de- and regeneration and correlated to clinical disease duration. 3C) histopathological severity was rated semi-quantitatively in mild, moderate and severe and assessed quantitatively by counting the large fiber density/mm^2. Electrophysiological parameters (SNAP) were assessed and compared in the three histopathological severity groups. The last column shows results of statistical testing between the groups using Kruskal-Wallis test with Dunn's correction for multiple testing if necessary (adjusted p-values are shown). Abbreviations: LLN = lower limit of normal, SNAP = Sensory nerve action potential.

medRxiv preprint doi: https://doi.org/10.1101/2022.08.05.22278366; this version posted November 8, 2022. The copyright holder for this preprint (which was not certified by peer review) is the author/funder, who has granted medRxiv a license to display the preprint in perpetuity. It is made available under a CC-BY 4.0 International license .

4 A) autocorrelation peak-to peak distance (periodicity)

protein	localization	mouse	human		p-value
			axonal	demyelinating	
ß2-spectrin	internode	187.54 ± 20.59	183.97 ± 12.96		0.18
			183.05 ± 13.87	187.72 ± 7.94	
			p = 0.89	p = 0.74	
ß2-spectrin	paranode	184.28± 16.04	197.35 ± 36.18		0.03
			201.81 ± 41.38	190.66 ± 27.46	
			p = 0.006	p = 1	
Caspr-1	paranode	186.63 ± 24.73	247.15 ± 98.668		< 0.0001
			256.16 ± 100.11	203.25 ± 78.73	
			p < 0.00001	p < 0.00001	
Pan-NF	paranode	173.16 ± 23.61	283.85 ± 124.63		< 0.0001
			283.27 ± 125.94	293.36 ± 106.13	
			p = p < 0.00001	p < 0.00001	

4 B) colocalization (Manders' A correlation coefficients)

protein 1	protein 2	mouse	human			p-value
			acute axonal	chronic axonal	demyelinating	
Caspr-1	ß2-spectrin	0.91 ± 0.05		0.76 ± 0.15		< 0.0001
			0.73 ± 0.18	0.79 ± 0.12	0.79 ± 0.13	
			p < 0.0001	p = 0.003	p = 0.002	
Caspr-1	neurofascin-155 (paranode)	0.90 ± 0.06		0.87 ± 0.07		0.93
			0.88 ± 0.06	0.87 ± 0.06	0.87 ± 0.1	
			p < 0.0001	p = 0.003	p = 0.002	

4 C) colocalization (Manders' B correlation coefficients)

protein 1	protein 2	mouse	human			p-value
			acute axonal	chronic axonal	demyelinating	
Caspr-1	ß2-spectrin	0.75 ± 0.18		0.55 ± 0.21		< 0.001
			0.48 ± 0.23	0.70 ± 0.17	0.53 ± 0.14	
			p < 0.0001	p = 1	p = 0.006	
Caspr-1	neurofascin-155 (paranode)	0.88 ± 0.07		0.84 ± 0.09		0.25
			0.84 ± 0.07	0.85 ± 0.07	0.82 ± 0.13	
			p < 0.52	p = 1	p = 0.72	

Table S4. *d*STORM imaging parameters in mice and patients with polyneuropathies.(A) Autocorrelation peak-to peak distances (periodicity) of internodal and paranodal ß2-spectrin, Caspr-1 and neurofascin-155 in mice and patients with polyneuropathies. (B-C): Colocalization analysis using Manders' A and B correlation coefficients between Caspr-1 with ß2-spectrin and with the paranodal fraction of pan-neurofascin (neurofascin-155) are displayed in mouse and human Nodes of Ranvier. P-values of Kruskal-Wallis test with Dunn's correction for multiple testing are shown in the right column (mouse vs. human) and below the individual results of subanalysis (mouse vs. human axonal / demyelinating neuropathy subcohort).

medRxiv preprint doi: https://doi.org/10.1101/2022.08.05.22278366; this version posted November 8, 2022. The copyright holder for this preprint (which was not certified by peer review) is the author/funder, who has granted medRxiv a license to display the preprint in perpetuity. It is made available under a CC-BY 4.0 International license .

no	n of measured nodes	nodal count	axonal paranodal diameter			nodo-paranodal length			nodal length		
		nodes/tissue volume (mm^3)	mean ± SD (µm)	median (µm)	adjusted p-value	mean ± SD (µm)	median (µm)	adjusted p-value	mean ± SD (µm)	median (µm)	adjusted p-value
1	40	16.91	2.74 ± 1.12	2.57	0.1072	13.09 ± 5.51	11.45	0.0006	1.17 ± 1.58	0.89	>0.9999
2*	40	21.53	2.85 ± 0.75	2.85	0.0004	14.11 ± 6.45	12.30	<0.0001	0.99 ± 0.81	0.79	>0.9999
3	40	18.32	2.16 ± 0.65	2.23	>0.9999	13.88 ± 7.74	10.40	0.0016	1.16 ± 0.33	1.10	0.1692
4	26	12.17	2.40 ± 0.96	2.46	>0.9999	12.21 ± 2.91	11.26	0.0032	0.91 ± 0.60	0.84	>0.9999
5	39	14.17	1.80 ± 0.66	1.64	0.1171	14.36 ± 6.66	12.25	<0.0001	1.23 ± 0.81	1.06	0.5359
6	37	13.22	2.08 ± 0.73	1.93	>0.9999	24.66 ± 17.64	15.99	<0.0001	2.16 ± 2.49	1.45	<0.0001
7	40	38.96	2.41 ± 0.95	2.26	>0.9999	12.99 ± 9.33	9.88	0.3935	1.73 ± 3.96	0.86	>0.9999
8*	40	30.12	2.16 ± 0.84	1.94	>0.9999	12.11 ± 6.11	10.65	0.0487	0.81 ± 0.49	0.70	>0.9999
9	22	18.28	2.61 ± 1.01	2.32	>0.9999	16.43 ± 10.16	13.16	0.0002	1.07 ± 0.83	0.78	>0.9999
10	38	28.67	2.26 ± 0.93	2.01	>0.9999	10.90 ± 3.35	10.74	0.2976	0.85 ± 0.34	0.78	>0.9999
11	40	36.37	2.03 ± 0.65	1.95	>0.9999	13.65 ± 8.22	11.53	0.0012	0.92 ± 1.59	0.59	0.2211
12*	40	47.41	1.79 ± 0.72	1.48	0.0652	11.29 ± 3.23	10.56	0.1324	0.92 ± 0.74	1.48	<0.0001
13	35	22.31	2.39 ± 0.93	2.23	>0.9999	14.96 ± 2.39	11.79	<0.0001	0.93 ± 0.59	0.76	>0.9999
14*	40	19.95	2.74 ± 1.14	2.57	0.334	10.46 ± 7.81	9.47	>0.9999	0.93 ± 0.93	0.71	>0.9999
15	40	21.80	3.14 ± 1.11	3.21	0.0001	11.49 ± 3.08	10.73	0.0231	1.32 ± 0.40	1.27	0.0008
16	30	82.68	2.86 ± 1.12	2.89	0.0651	14.00 ± 6.67	11.53	0.0008	1.16 ± 1.75	0.65	>0.9999
17	235	32.51	2.24 ± 0.58	2.20	>0.9999	14.35 ± 8.26	12.80	<0,0001	1.23 ± 0.52	1.16	0.0727

Table S5. Morpometics at the Node: High content confocal imaging and analysis data in single patients. Means ± standard deviations and medians of nodo-paranodal parameters (nodes / tissue volume, axonal paranodal diameter, nodo-paranodal length, nodal length) are shown for single patients of the cohort. Adjusted p-values are displayed compared to intact human nerves using Kruskal-Wallis test with Dunn's correction for multiple testing. Patient biopsies that were used to select intact nodes are marked with asterisks. Abbreviations: no = number, SD standard deviation.

medRxiv preprint doi: https://doi.org/10.1101/2022.08.05.22278366; this version posted November 8, 2022. The copyright holder for this preprint (which was not certified by peer review) is the author/funder, who has granted medRxiv a license to display the preprint in perpetuity. It is made available under a CC-BY 4.0 International license .

Parameter [unit]	Values
angle of antibodies [degree]:	90.00
sigma of antibodies deviation [degree]:	0.00
binding sites per nm [nm^{-1}]:	0.05
labeling efficiency [%]:	10, 25, 50, 75, 100
radius of filament [nm]:	12.5
fluorophores per label:	2.0
label epitope distance [nm]:	20.0
localization precision (sigma x,y) [nm]:	20.0
localization precision (sigma z) [nm]:	70.0
binding sites per square nanometer [nm^{-2}]:	0.016666668
frames:	20000
duty cycle:	5.0E-4
bleaching constant [1/10000 frames]:	2.231E-5
median photon number:	4000
detection efficiency [%]:	50.0
background events per volume [$1/m^3$]:	25, 50, 75, 100
FWHM of PSF [nm]:	647.0
pixel size for output images in nm:	10.0

Table S6. Summary of the parameters for the simulation of SMLM datasets of ground truth periodic line patterns with SuReSim. The parameter sets used in the sweep are highlighted in gray.

target protein (conjugate)	host	dilution	company	catalogue number
pan-neurofascin	polyclonal chicken IgY	0.4 µg/ml	R & D Systems	AF3235
Caspr-1	polyclonal rabbit IgG	0.2 µg/ml	Abcam	ab34151
b2-Spectrin II	monoclonal mouse IgG	5 µg/ml	BD Biosciences	612563
Myelin basic protein	monoclonal rat IgG	10 µg/ml	Abcam	ab7349
chicken IgY(Alexa 647)	polyclonal goat IgG	10 µg/ml	Invitrogen	A-21449
rabbit IgG (Alexa532)	polyclonal goat IgG	10 µg/ml	Invitrogen	A-11009
rat IgG (Alexa488)	polyclonal donkey IgG	3.75 µg/ml	Jackson IR	712-545-150
rabbit IgG (Cy3)	polyclonal donkey IgG	5 µg/ml	Jackson IR	711-165-152

Table S7. Antibodies used for fluorescence stainings

medRxiv preprint doi: https://doi.org/10.1101/2022.08.05.22278366; this version posted November 8, 2022. The copyright holder for this preprint (which was not certified by peer review) is the author/funder, who has granted medRxiv a license to display the preprint in perpetuity. It is made available under a CC-BY 4.0 International license .

Illumination	640 nm laser (iBEAM-smart-640-S, Toptica) 532 nm laser (GEM 532 nm, 250 mW, Laser Quantum)
Clean up filters	640/8 nm MaxDiode™ laser clean-up, Semrock Filter ZET 532/10 clean-up, Chroma
Dichroic filter	QuadLine Laser-Beamsplitter R405/488/532/635, Semrock Quad-Notch Filter 405/488/532/635, Semrock
Two-channel detection	Optosplit II (Crain) with Beamsplitter T 635 LPXR, Semrock
Emission filters	BrightLine HC 593/40, Semrock 700/75 ET, Chroma
Camera	iXon ultra DU-897U-CSO-BV, Andor

Table S8. Customized two-color *d*STORM microscope specifications.

parameter	Zeiss LSM 980 Airyscan 2	Zeiss Observer Z.1, Carl Zeiss AG
objective	Plan-Apochromat 20x/0.8 M27 objective	Alpha Plan-Apochromat 63x NA 1.46 Oil Korr, 420780-9970
detector/camera	GaAsP-PMT 747V detector gain, offset, digital gain 1.0	EMCCD Camera EM-Gain: 100, 17.7 photoelectrons per A/D count
pixels per FoV	2658*2658	170*170
Z-stacks	44 slices	-
voxels/pixel size	x,y = 74 nm & z=350 nm	x,y =103 nm
laser excitation	488 nm, 561 nm & 639 nm	532 nm, 639 nm 1-5 kW cm2
channels	sequential Ch1: 420-480nm/495-550nm for 488 nm Ch2: 300-720nm Ch3: 300-720nm	sequential Ch1: 663-738 nm Ch2: 573-613 nm
acquisition	speed: 0.37 µs per pixel bidirectional scanning pinhole: 11.14 (Ch1)/10.50(Ch2) /9.9(Ch3) Airy units	20000 fr 7 ms (Ch1)/13 ms (Ch 2) exposure time
image processing	Zen blue 3.3 (Carl Zeiss AG) a) tiling & stitching 4 times 1*9, 3*3 or 5*2 tiling, fuse tiles, minimal overlap 5%, maximal shift 10% b) Airyscan processing 3D processing, Auto Filer, strength: standard	ThunderSTORM: Image filtering: Wavelet filter(B-spline), order: 3, scale: 2.0; Approximate localization of molecules: Local maximum, peak intensity threshold: x*std(Wave.F1) (x= 1.25-6), 8-neighborhood. Sub-pixel localizations of molecules: Integrated gaussian PSF, fitting radius [px]: 3, weighted least squares, initial sigma [px]: 1.6. Drift correction was performed with gold nanorods as fiducial markers, when visible in the field of view. Filters: 1 nm < uncertainty < 30 nm, 5 < intensity < 2500 photons

Table S9. Acquisition parameters and image processing details. Abbreviations: n/a: not applicable.

medRxiv preprint doi: https://doi.org/10.1101/2022.08.05.22278366; this version posted November 8, 2022. The copyright holder for this preprint
(which was not certified by peer review) is the author/funder, who has granted medRxiv a license to display the preprint in perpetuity.
It is made available under a CC-BY 4.0 International license .

Supplementary Figure 1-4

medRxiv preprint doi: https://doi.org/10.1101/2022.08.05.22278366; this version posted November 8, 2022. The copyright holder for this preprint (which was not certified by peer review) is the author/funder, who has granted medRxiv a license to display the preprint in perpetuity. It is made available under a CC-BY 4.0 International license .

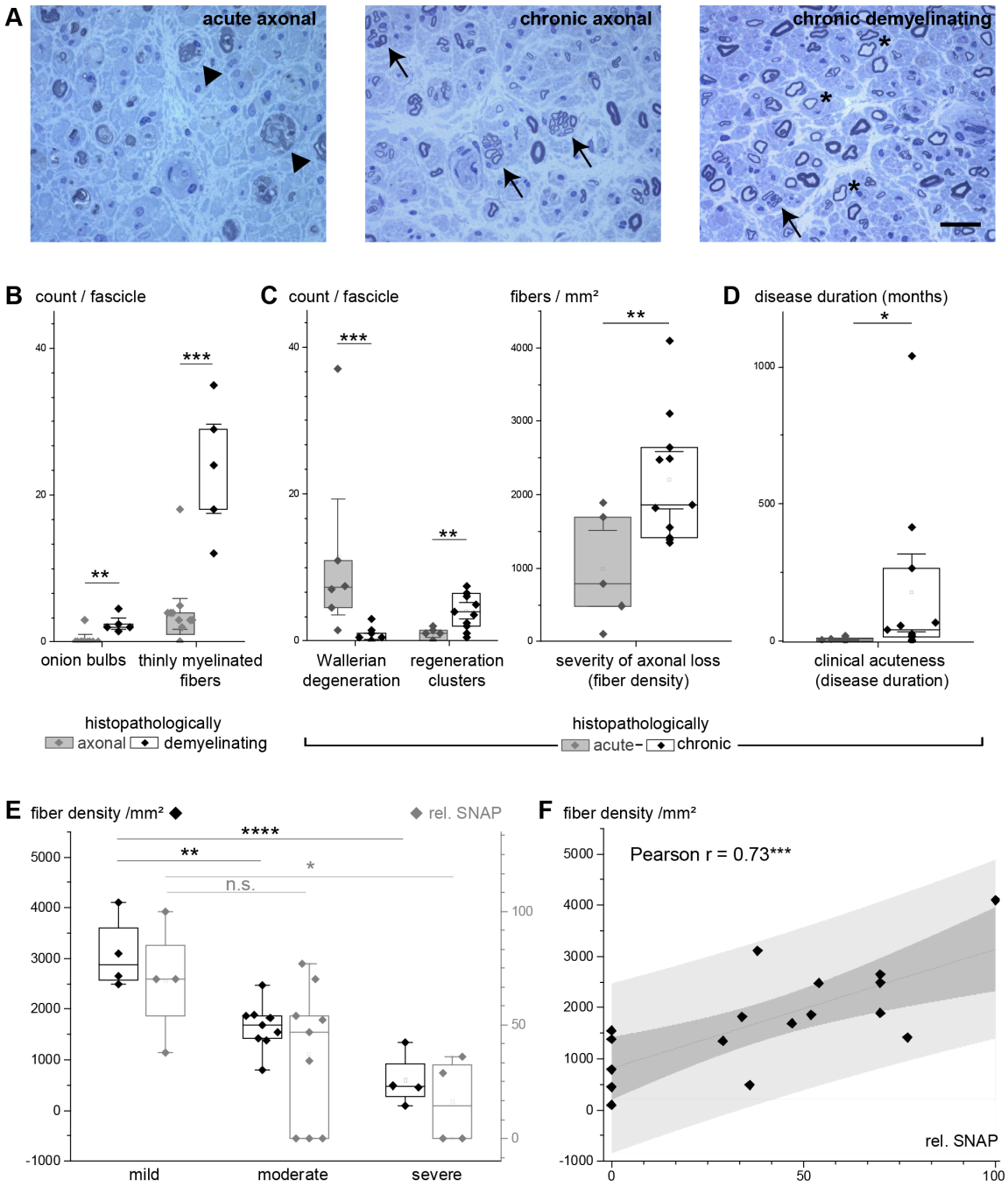

Fig. S1. Histopathological assessment of cross-sectional sensory nerve biopsies and validation. (A) Sensory nerve semithin cross sections with toluidine blue staining in acute axonal neuropathy, chronic axonal neuropathy and demyelinating neuropathy (left to right) show axonal loss with actively degeneration fibers (arrowheads, left) in acute axonal neuropathy, clusters of regenerating fibers in chronic axonal and demyelinating neuropathy (arrows) and thinly myelinated fibers in demyelinating neuropathy (asterisks). Scale bar = 20µm. (B) Histopathological classification by type of disease was validated by comparing the counts per fascicle (y-axis) of onion bulbs and thinly myelinated fibers (x-axis) between biopsies rated as axonal (gray) and demyelinating (black/white, see legend) using Mann-Whitney test. (C) Histopathological classification by acuteness was validated by comparing the counts / fascicle (left graph, y-axis) of Wallerian degeneration figures and regeneration clusters (left graph, x-axis) between biopsies rated as acute (gray) and chronic (black/white, see legend). Fiber density /mm^2 as an indicator of severity of axonal loss (right graph, y-axis) was significantly reduced in acute vs. chronic neuropathy (Student's t test). (D) Histopathological classification was clinically validated by comparing the clinical disease duration in acute vs. chronic neuropathy using Mann-Whitney test. (E-F) Histopathologic classification by severity was validated by nerve conduction studies data (exact values see Supplemental Table 3). (E) Fiber density /mm^2 (left y-axis, black) and relative SNAP in percent of the age-adjusted lower limit of normal (right y-axis, gray) significantly differ according to the severity of axonal loss, assessed by one-way ANOVA with Bonferroni adjustment (fiber density) and Welch one way ANOVA with Dunnett's T3 multiple comparison test (SNAP). (F) Relative SNAP (x-axis) correlated positively to the fiber density (y-axis) using Pearson's correlation coefficient. Significance level: * $p < 0.05$. ** $p < 0.01$, *** $p < 0.001$, **** $p < 0.0001$. Abbreviations: n.s. = not significant, SNAP = sensory nerve action potential.

medRxiv preprint doi: https://doi.org/10.1101/2022.08.05.22278366; this version posted November 8, 2022. The copyright holder for this preprint (which was not certified by peer review) is the author/funder, who has granted medRxiv a license to display the preprint in perpetuity. It is made available under a CC-BY 4.0 International license .

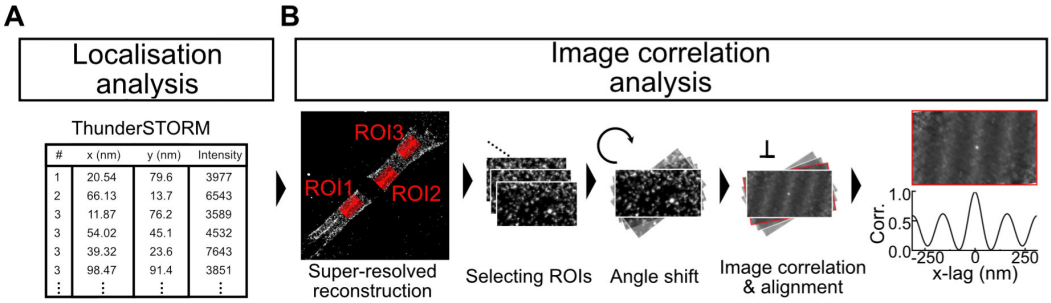

Fig. S2. Image reconstruction and analysis workflow. (A) The ThunderSTORM localisation analysis of the SMLM image sequences provides a list of molecule positions. Based on this list, a super-resolved image of ultrastructural organization of the protein of interest at the node of Ranvier is reconstructed. (B) The Image correlation analysis is performed with a custom MatLab tool which allows to select regions of interest in the super-resolved image. The ROIs are rotated in steps before image auto-correlation to align the pattern perpendicular to the horizontal axis.

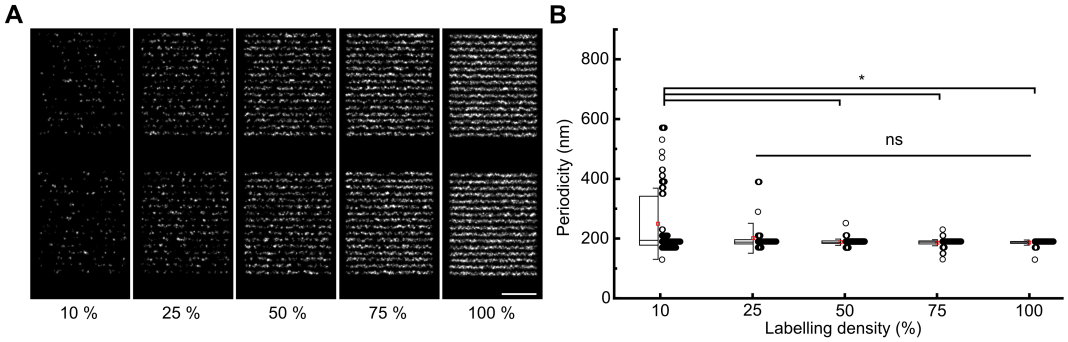

Fig. S3. Super-resolution image autocorrelation analysis robustly identifies structural periodicity in the case of incomplete labeling. (A) Based on super-resolved reconstructions of simulated SMLM data of a ground truth line structure with 190 nm periodicity and labeling densities from 10 to 100%, autocorrelation (B) successfully retrieves the periodicity spacing at minimum 25% (median ± standard deviation; 10%:194 ± 119 nm, n = 91; 25%: 188 ± 50 nm, n = 94; 50%: 186 ± 11 nm, n = 131; 75%: 188 ± 11 nm, n = 150; 100%: 188 ± 9 nm, n = 134; Kruskal-Wallis test). Scale bar 1 µm.

medRxiv preprint doi: https://doi.org/10.1101/2022.08.05.22278366; this version posted November 8, 2022. The copyright holder for this preprint (which was not certified by peer review) is the author/funder, who has granted medRxiv a license to display the preprint in perpetuity. It is made available under a CC-BY 4.0 International license .

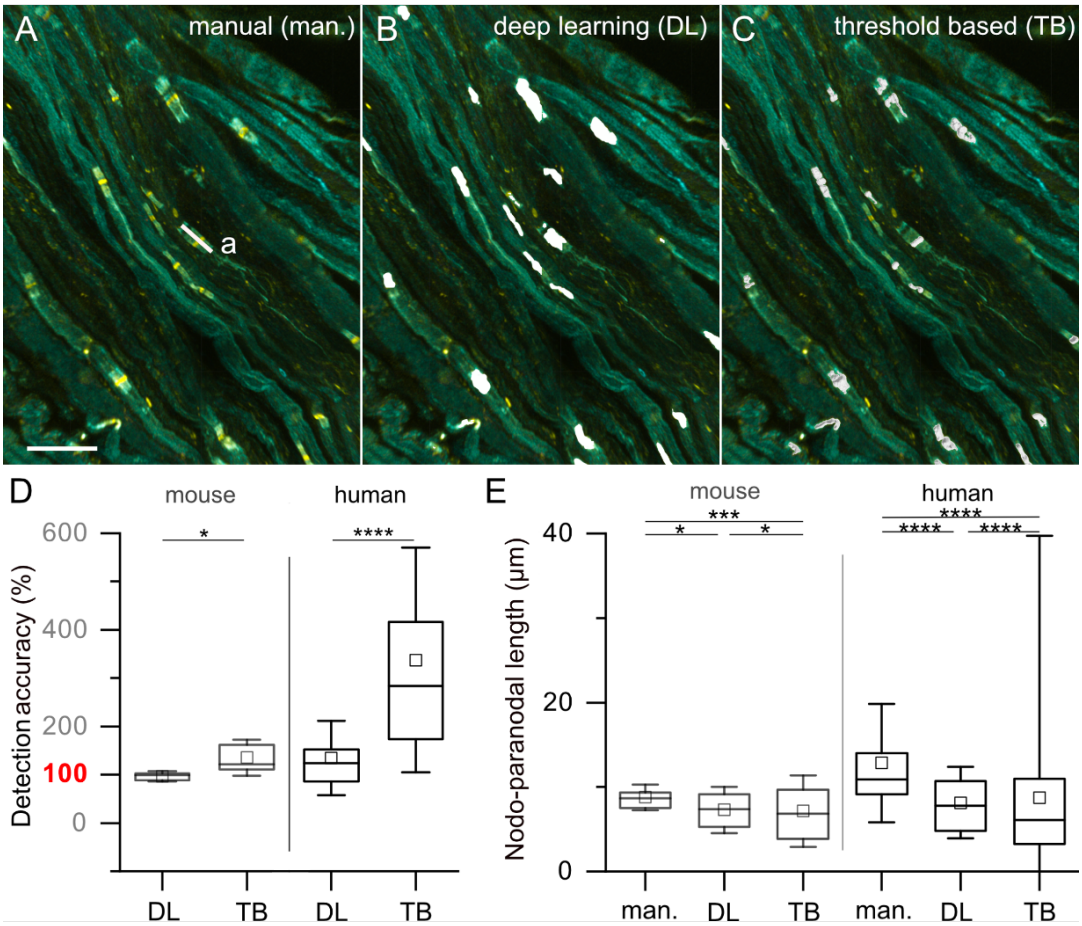

Fig. S4. Assessment of node detection and nodo-paranodal length by deep learning based segmentation vs. threshold based segmentation. (A-C) Murine ischiadic nerve teased fiber preparations with two-color labeling (pan-neurofascin in yellow and Caspr-1 in cyan, A) were segmented using deep learning (DL, B) or threshold based segmentation using Imaris Software (TB, C) to identify single nodes of Ranvier. Scale bar = 20 µm. (D) Detection and counting accuracy of the nodes of Ranvier using DL vs TB. In both mouse and human samples DL performed significantly better than TB in detecting nodes of Ranvier, using manual assessment as a reference. Median ± std deviation in mouse was 0.99 ± 0.1 vs 1.21 ± 1.36, $p = 0.046$ and in human 1.21 ± 0.77 vs 2.83 ± 2.33 $p < 0.0001$, determined by Kruskal-Wallis ANOVA with adjustment for multiple testing. (E) Nodo-paranodal length calculated from DL and Imaris threshold based image segmentation was compared to manual ROI definition using FIJI by two independent and blinded investigators. Data were compared in murine and human samples. In both, statistically significant differences between automated and manual analysis could be detected. In both cases, results from image segmentation with DL were closer to manual assessment than threshold based assessment (median ± std deviation nodo-paranodal length in µm in mouse: man.: 8.6 ± 1.5, DL: 7.2 ± 2.7 $p = 0.02$, TB: 6.9 ± 4.2 $p < 0.0001$, human: man.: 10.9 ± 7.0, DL: 7.8 ± 4.2 $p < 0.001$, TB: 6.1 ± 31.0 $p < 0.0001$, calculated by Kruskal-Wallis ANOVA with adjustment for multiple testing. Significance level: * $p < 0.05$. ** $p < 0.01$, *** $p < 0.001$, **** $p < 0.0001$.

medRxiv preprint doi: https://doi.org/10.1101/2022.08.05.22278366; this version posted November 8, 2022. The copyright holder for this preprint (which was not certified by peer review) is the author/funder, who has granted medRxiv a license to display the preprint in perpetuity. It is made available under a CC-BY 4.0 International license .

Supplementary Movies

Supplementary Movie M1: Assessment of nodo-paranodal parameters based on multicolor large field of view fluorescence imaging. Human sural nerve teased fiber preparations with triple-labeling (MBP in magenta, pan-neurofascin in yellow and Caspr-1 in cyan) were imaged to asses the nodo-paranodal length, paranodal diameter and nodeal gap as indicated in the video. Scale bar = 100 µm.

Supplementary Bibliography

1. Peter Y. K. Van den Bergh, Pieter A. Doorn, Robert D. M. Hadden, Bert Avau, Patrik Vankrunkelsven, Jeffrey A. Allen, Shahram Attarian, Patricia H. Blomkwist-Markens, David R. Cornblath, Filip Eftimov, H. Stephan Goedee, Thomas Harbo, Satoshi Kuwabara, Richard A. Lewis, Michael P. Lunn, Eduardo Nobile-Orazio, Luis Querol, Yusuf A. Rajabally, Claudia Sommer, and Haluk A. Topaloglu. European academy of neurology/peripheral nerve society guideline on diagnosis and treatment of chronic inflammatory demyelinating polyradiculoneuropathy: Report of a joint task force—second revision. 26(3):242–268. ISSN 1085-9489, 1529-8027. doi: 10.1111/jns.12455.
2. Angela Dispenzieri. POEMS syndrome: 2017 update on diagnosis, risk stratification, and management: DISPENZIERI. 92(8):814–829. ISSN 03618609. doi: 10.1002/ajh.24802.
3. Michael P. Collins, P. James B. Dyck, Gary S. Gronseth, Loïc Guillevin, Robert D. M. Hadden, Dieter Heuss, Jean-Marc Léger, N.C. Notermans, John D. Pollard, Gérard Said, Gen Sobue, A.F.J.E. Vrancken, and John T. Kissel. Peripheral nerve society guideline* on the classification, diagnosis, investigation, and immunosuppressive therapy of non-systemic vasculitic neuropathy: executive summary. 15(3):176–184. ISSN 10859489. doi: 10.1111/j.1529-8027.2010.00281.x.
4. I S J Merkies. Clinimetric evaluation of a new overall disability scale in immune mediated polyneuropathies. 72(5):596–601. ISSN 00223050. doi: 10.1136/jnnp.72.5.596.
5. Ruud P. Kleyweg, Frans G. A. Van Der Meché, and Paul I. M. Schmitz. Interobserver agreement in the assessment of muscle strength and functional abilities in guillain-barré syndrome: Muscle strength assessment in GBS. 14(11):1103–1109. ISSN 0148639X. doi: 10.1002/mus.880141111.
6. Peter J. Dyck, P. James B. Dyck, and Janean Engelstad. Pathologic alterations of nerves. In *Peripheral Neuropathy*, pages 733–829. Elsevier, . ISBN 978-0-7216-9491-7. doi: 10.1016/B978-0-7216-9491-7.50035-1.
7. M.D. Abramoff, Paulo J. Magalhães, and Sunanda J. Ram. Image processing with ImageJ. 11(7):36–42. ISSN 1081-8693.
8. Johannes Schindelin, Ignacio Arganda-Carreras, Erwin Frise, Verena Kaynig, Mark Longair, Tobias Pietzsch, Stephan Preibisch, Curtis Rueden, Stephan Saalfeld, Benjamin Schmid, Jean-Yves Tinevez, Daniel James White, Volker Hartenstein, Kevin Eliceiri, Pavel Tomancak, and Albert Cardona. Fiji: an open-source platform for biological-image analysis. 9(7):676–682. ISSN 1548-7091, 1548-7105. doi: 10.1038/nmeth.2019.
9. Adam Paszke, Sam Gross, Francisco Massa, Adam Lerer, James Bradbury, Gregory Chanan, Trevor Killeen, Zeming Lin, Natalia Gimelshein, Luca Antiga, Alban Desmaison, Andreas Köpf, Edward Yang, Zach DeVito, Martin Raison, Alykhan Tejani, Sasank Chilamkurthy, Benoit Steiner, Lu Fang, Junjie Bai, and Soumith Chintala. PyTorch: An imperative style, high-performance deep learning library. doi: 10.48550/ARXIV.1912.01703. Publisher: arXiv Version Number: 1.
10. Kaiming He, Xiangyu Zhang, Shaoqing Ren, and Jian Sun. Deep residual learning for image recognition. doi: 10.48550/ARXIV.1512.03385. Publisher: arXiv Version Number: 1.
11. Ismail M. Khater, Ivan Robert Nabi, and Ghassan Hamarneh. A review of super-resolution single-molecule localization microscopy cluster analysis and quantification methods. 1(3):100038. ISSN 26663899. doi: 10.1016/j.patter.2020.100038.
12. Viktor Toth, Naveen Jayaprakash, Adam Abbas, Ariba Khan, Stavros Zanos, and Theodoros P. Zanos. Single-axon level automatic segmentation and feature extraction from immuhistochemical images of peripheral nerves. In *2020 42nd Annual International Conference of the IEEE Engineering in Medicine & Biology Society (EMBC)*, pages 1859–1862. IEEE. ISBN 978-1-72811-990-8. doi: 10.1109/EMBC44109.2020.9175974.
13. De-En Xu, Wen-Min Zhang, Zara Zhuyun Yang, Hong-Mei Zhu, Ke Yan, Shao Li, Dominique Bagnard, Gavin S Dawe, Quan-Hong Ma, and Zhi-Cheng Xiao. Amyloid precursor protein at node of ranvier modulates nodal formation. 8(4):396–403. ISSN 1933-6918, 1933-6926. doi: 10.4161/cam.28802.
14. Aldo Zaimi, Maxime Wabartha, Victor Herman, Pierre-Louis Antonsanti, Christian S. Perone, and Julien Cohen-Adad. AxonDeepSeg: automatic axon and myelin segmentation from microscopy data using convolutional neural networks. 8(1):3816. ISSN 2045-2322. doi: 10.1038/s41598-018-22181-4.
15. Chuansheng Zhang, Keiichiro Susuki, Daniel R. Zollinger, Jeffrey L. Dupree, and Matthew N. Rasband. Membrane domain organization of myelinated axons requires βII spectrin. 203(3):437–443. ISSN 1540-8140, 0021-9525. doi: 10.1083/jcb.201308116.
16. Iván Coto Hernández, Suresh Mohan, Steven Minderler, and Nate Jowett. Super-resolved fluorescence imaging of peripheral nerve. 12(1):12450. ISSN 2045-2322. doi: 10.1038/s41598-022-16769-0.
17. Z. Cai, J.W. Finnie, P.C. Blumbergs, J. Manavis, M.N. Ghabriel, and P.D. Thompson. Early paranodal myelin swellings (tomacula) in an avian riboflavin deficiency model of demyelinating neuropathy. 198(1):65–71. ISSN 00144886. doi: 10.1016/j.expneurol.2005.10.028.
18. G. Wolswijk. Changes in the expression and localization of the paranodal protein caspr on axons in chronic multiple sclerosis. 126(7):1638–1649. ISSN 1460-2156. doi: 10.1093/brain/awg151.
19. Kathrin Doppler, Christian Werner, and Claudia Sommer. Disruption of nodal architecture in skin biopsies of patients with demyelinating neuropathies. 18(2):168–176, . ISSN 10859489. doi: 10.1111/jns5.12023.
20. Claudia Schwab, Vimala Bondada, D. Larry Sparks, Leslie D. Cahan, and James W. Geddes. Postmortem changes in the levels and localization of microtubule-associated proteins (tau, MAP2 and MAP1b) in the rat and human hippocampus. 4(2):210–225. ISSN 1050-9631, 1098-1063. doi: 10.1002/hipo.450040212.
21. Peter James Dyck, Alfred Lais, Jeannine L. Karnes, Peter O'Brien, and Robert Rizza. Fiber loss is primary and multifocal in sural nerves in diabetic polyneuropathy. 19(5):425–439, . ISSN 0364-5134, 1531-8249. doi: 10.1002/ana.410190503.
22. Marilyne Labasque, Bruno Hivert, Gisela Nogales-Gadea, Luis Querol, Isabel Illa, and Catherine Faivre-Sarrailh. Specific contactin n-glycans are implicated in neurofascin binding and autoimmune targeting in peripheral neuropathies. 289(11):7907–7918. ISSN 00219258. doi: 10.1074/jbc.M113.528489.
23. Constance Manso, Luis Querol, Cinta Lleixà, Mallory Poncelet, Mourad Mekaouche, Jean-Michel Vallat, Isabel Illa, and Jérôme J. Devaux. Anti–neurofascin-155 IgG4 antibodies prevent paranodal complex formation in vivo. 129(6):2222–2236, . ISSN 0021-9738, 1558-8238. doi: 10.1172/JCI124694.
24. Constance Manso, Luis Querol, Mourad Mekaouche, Isabel Illa, and Jérôme J. Devaux. Contactin-1 IgG4 antibodies cause paranode dismantling and conduction defects. 139(6):1700–1712, . ISSN 0006-8950, 1460-2156. doi: 10.1093/brain/aww062.
25. Jean-Michel Vallat, Laurent Magy, Philippe Corcia, Jean-Marc Boulesteix, Antonino Uncini, and Stéphane Mathis. Ultrastructural lesions of nodo-paranodopathies in peripheral neuropathies. 79(3):247–255, . ISSN 0022-3069, 1554-6578. doi: 10.1093/jnen/nlz134.
26. Antonino Uncini, Stephane Mathis, and Jean-Michel Vallat. New classification of autoimmune neuropathies based on target antigens and involved domains of myelinated fibres. 93(1):57–67. ISSN 0022-3050, 1468-330X. doi: 10.1136/jnnp-2021-326889.
27. Kathrin Doppler, Christian Werner, Carsten Henneges, and Claudia Sommer. Analysis of myelinated fibers in human skin biopsies of patients with neuropathies. 259(9):1879–1887, . ISSN 0340-5354, 1432-1459. doi: 10.1007/s00415-012-6432-7.
28. Claudia Sommer. Nerve and skin biopsy in neuropathies. 31(5):534–540. ISSN 1350-7540, 1473-6551. doi: 10.1097/WCO.0000000000000601.
29. Haruki Koike, Masato Kadoya, Ken-ichi Kaida, Shohei Ikeda, Yuichi Kawagashira, Masahiro Iijima, Daisuke Kato, Hidenori Ogata, Ryo Yamasaki, Noriyuki Matsukawa, Jun-ichi Kira, Masahisa Katsuno, and Gen Sobue. Paranodal dissection in chronic inflammatory demyelinating polyneuropathy with anti-neurofascin-155 and anti-contactin-1 antibodies. 88(6):465–473. ISSN 0022-3050, 1468-330X. doi: 10.1136/jnnp-2016-314895.
30. Jean-Michel Vallat, Mathilde Nizon, Alex Magee, Bertrand Isidor, Laurent Magy, Yann Péréon, Laurence Richard, Robert Ouvrier, Benjamin Cogné, Jérôme Devaux, Stephan Zuchner, and Stéphane Mathis. Contactin-associated protein 1 (*CNTNAP1*) mutations induce characteristic lesions of the paranodal region. 75(12):1155–1159, . ISSN 0022-3069, 1554-6578. doi: 10.1093/jnen/nlw093.
31. Jean-Michel Vallat, Nobuhiro Yuki, Kenji Sekiguchi, Norito Kokubun, Nobuyuki Oka, Stéphane Mathis, Laurent Magy, Diane L. Sherman, Peter J. Brophy, and Jérôme J. Devaux. Paranodal lesions in chronic inflammatory demyelinating polyneuropathy associated with anti-neurofascin 155 antibodies. 27(3):290–293, . ISSN 09608966. doi: 10.1016/j.nmd.2016.10.008.